

Determining conditions that allow a shear margin to coincide with a R thlisberger channel

John D. Platt^{1,2}, Thibaut Perol,¹ Jenny Suckale³, and James R. Rice^{1,4}

Information for published version (essentially identical text and graphics as in this version):

Citation:

Platt, J. D., T. Perol, J. Suckale, and J. R. Rice (2016), Determining conditions that allow a shear margin to coincide with a R thlisberger channel, *J. Geophys. Res. Earth Surf.*, 121, doi:10.1002/2015JF003707. Received 26 AUG 2015. Accepted 30 MAY 2016, Accepted article online 7 JUN 2016

¹Harvard John A. Paulson School of
Engineering and Applied Sciences, Harvard
University, Cambridge, Massachusetts,
USA.

²Now at, Department of Terrestrial
Magnetism, Carnegie Institution for
Science, Washington DC, USA.

³Department of Geophysics, Stanford
University, Palo Alto, California, USA.

⁴Department of Earth and Planetary
Sciences, Harvard University, Cambridge,
Massachusetts, USA.

Abstract.

The mass loss from the West Antarctic Ice Sheet is dominated by numerous rapidly flowing ice streams, which are separated from stagnant ice in the adjacent ridges by zones of concentrated deformation known as shear margins. Because the discharge from a single ice stream depends sensitively on the ice stream width, determining the physical processes that control shear margin location is crucial to a full understanding of ice stream dynamics. Previous work has shown that the transition from a deforming to an undeforming bed within a shear margin concentrates large stresses on the undeforming bed beneath the ridge [Jacobson and Raymond, 1998; Schoof, 2004; Suckale *et al.*, 2014]. In this paper we investigate how the presence of a drainage channel collocated with the transition from a deforming to an undeforming bed perturbs the stress field within the shear margin. We show that the channel limits the maximum shear stress on the undeforming bed and alters the yield strength of the till by changing the normal stress on the ice-till interface. By comparing the maximum stress with the till strength, we show that the transition from a deforming to an undeforming bed can occur across a channel whenever the water flux in the channel exceeds a critical value. This critical flux is sensitive to the rheology and loading of the shear margin, but we conclude that there are some scenarios where the transition from a deforming to an undeforming bed can be collocated with a drainage channel, though this configuration is probably not typical.

1. Introduction

23 Surface velocity observations of the West Antarctic Ice Sheet show that ice flow is highly
24 non-uniform, with regions of $\sim 20-80$ km width known as ice streams flowing much faster
25 than the surrounding ice sheet. Despite accounting for a fraction of the surface area of
26 the ice sheet, rapidly flowing ice streams dominate the discharge of ice from the continent
27 [*Bamber et al.*, 2000]. Thus, determining the physical processes that govern ice stream
28 dynamics is of the utmost importance to understanding how West Antarctica will respond
29 to a changing climate.

30 Typically ice streams have an ice thickness of one kilometer, a width of a few tens of
31 kilometers, and a length of a few hundred kilometers. The surface velocity in the center
32 of an ice stream is a few hundreds of meters per year, which is significantly larger than
33 the surface velocity of a few meters per year in the surrounding ice sheet. Rapid flow is
34 possible despite the low gravitational stress driving deformation (~ 10 kPa) because of
35 the presence of a saturated subglacial till layer beneath the ice stream [*Blankenship et al.*,
36 1986, 1987]. The pore pressure in the till layer is close to the ice overburden, leading to
37 a low effective stress. For the Coulomb-plastic rheology typically observed in laboratory
38 experiments on subglacial till [*Kamb*, 1991; *Iverson et al.*, 1998; *Tulaczyk et al.*, 2000],
39 a low effective stress produces a low yield strength. Thus, the subglacial till provides
40 limited resistance to flow and a substantial fraction of the ice stream surface velocity is
41 accommodated by till deformation [*Alley et al.*, 1986].

42 A zone of concentrated deformation known as a shear margin separates the rapidly
43 flowing ice stream from the stagnant ice in the adjacent ridge. Shear margins are typ-

44 ically a few kilometers wide and marked by extensive surface crevassing [*Bindschadler*
45 *and Vornberger*, 1990; *Echelmeyer et al.*, 1994; *Scambos et al.*, 1994]. Because the till
46 provides limited resistance to motion, shear margins balance a substantial fraction of the
47 gravitational driving stress [*Echelmeyer et al.*, 1994; *Jackson and Kamb*, 1997; *Harrison*
48 *et al.*, 1998; *Joughin et al.*, 2002]. The shear margin location also sets the width of the ice
49 stream, and thus plays an important role in determining the ice stream discharge [*van der*
50 *Veen and Whillans*, 1996; *Raymond*, 1996; *Raymond et al.*, 2001]. Despite the important
51 role shear margins play in ice stream dynamics, the physical processes that select their
52 location are still uncertain. In contrast with mountain glaciers, topography alone does
53 not appear to explain current shear margin locations of Siple Coast ice streams [*Shabtaie*
54 *and Bentley*, 1987, 1988; *Raymond et al.*, 2001], and thus shear margin location in this
55 case must depend on the mechanical properties of ice and till.

56 Within a shear margin, there must be a transition from a deforming bed beneath an ice
57 stream, where the stress on the bed reaches the yield strength of the subglacial till and
58 plastic deformation occurs, to an undeforming bed beneath the ridge, where the stress is
59 always less than the yield strength of the till. Henceforth we refer to the point where this
60 transition occurs as the locking point. For ice streams where the shear margins support
61 a substantial fraction of the gravitational driving stress the mechanical transition at the
62 locking point concentrates stress on the undeforming bed, so for a shear margin to exist
63 there must be a mechanism that raises the yield strength of the undeforming bed far above
64 the yield strength inferred beneath the majority of the ice stream. One strengthening
65 mechanism that is commonly appealed to is freezing of the subglacial till, as studied by
66 *Jacobson and Raymond* [1998], *Schoof* [2012], and *Haseloff* [2015]. Alternatively, *Perol et*

67 *al.* [2015] proposed that melt generated by concentrated deformation in the shear margins
68 feeds a subglacial drainage channel at the base of the shear margin. This drainage channel
69 allows more efficient drainage than the distributed hydrologic system that operates under
70 the remainder of the ice stream, and decreases the pore pressure in a zone of kilometer-
71 scale width within the shear margin. For a Coulomb-plastic rheology, reducing the pore
72 pressure raises the yield strength of the till, allowing a stable margin configuration to form
73 if the locking point is not collocated with the channel. Here we define a stable margin
74 configuration to be one for which the shear stress resolved on the bed is less than the
75 yield strength of the till wherever the bed is undeforming. We use the term stable to
76 describe such a configuration because if the stress exceeds the strength anywhere on the
77 undeforming bed then that portion of the bed will yield and the ice stream will widen.

78 In this paper we investigate under what conditions the locking point can be collocated
79 with a drainage channel. This analysis complements *Perol et al.* [2015], which investi-
80 gated how a drainage channel not collocated with the locking point can select the margin
81 location. The crucial consideration in this manuscript is how the presence of a channel
82 alters the stress field around the locking point, while *Perol et al.* [2015] primarily focused
83 on how the channel raises the yield strength of the till over a broad zone within the shear
84 margin. To begin we show that a sharp transition (i.e. no drainage channel) generally
85 leads to a singular stress profile on the undeforming bed, an obviously unphysical scenario
86 because the yield strength of the undeforming bed is finite. Next we show that the pres-
87 ence of a channel at the locking point limits the maximum shear stress on the undeforming
88 bed and alters the yield strength of the till by changing the normal stress on the ice-till
89 interface. Comparing the maximum stress on the undeforming bed with the till strength

90 we investigate when the locking point can be collocated with a channel. Our results lead
91 to a critical water flux in the channel that must be exceeded for the transition from a
92 deforming to an undeforming bed to occur across a channel. For a Glen’s law rheology this
93 critical flux is unrealistically large if the average lateral shear stress in the shear margin
94 exceeds $\sim 35 - 50$ kPa. However, for the dislocation creep rheology of *Durham et al.*
95 [1997], which is governed by a stress exponent of four, that dominates near the transition
96 from a deforming to an undeforming bed if grain sizes are greater than a few millimeters
97 (for smaller grain sizes deformation falls into the grain boundary sliding regime explored
98 in *Goldsby and Kohlstedt* [2001]) the critical flux is substantially lower, and the locking
99 point can be collocated with the channel if the average lateral shear stress in the shear
100 margin is less than $\sim 85 - 115$ kPa. Using data for a range of shear margins from *Joughin*
101 *et al.* [2002], *Perol and Rice* [2015] estimated that $\tau_{lat} \approx 100 - 135$ kPa. Thus, we conclude
102 that there are some scenarios where the locking point can be collocated with a drainage
103 channel, though this configuration is probably not typical.

104 Though this manuscript revolves around a subglacial drainage channel, one of the key
105 elements in many subglacial hydrology models, our focus is not on modeling how large
106 scale variations in subglacial hydrology influence ice stream dynamics. Instead, we focus
107 on how the presence of a drainage channel alters the stress field at the base of a shear
108 margin on length scales of a few tens of meters. These length scales are small enough that
109 spatial variations in pore pressure are negligible if we assume typical permeabilities for
110 subglacial till. Our results show that the transition from a deforming to an undeforming
111 bed within a shear margin can occur across a channel if the water flux in the channel
112 exceeds a critical value, providing a natural path to incorporating our work into larger

113 scale models of subglacial hydrology. Our work complements several recent papers that
 114 focus on how large scale variations in subglacial hydrology influence ice sheet dynamics
 115 on a range of time and length scales. Most closely related to our work, *Perol et al.* [2015]
 116 showed that the presence of drainage channel can select the location of the locking point
 117 by raising the yield strength of the till over a broad zone within the shear margin. On a
 118 larger scale, *Kyrke-Smith et al.* [2014] and *Kyrke-Smith et al.* [2015] investigated how the
 119 coupling between ice flow and subglacial hydrology controls the formation and spacing of
 120 ice streams. Finally, on a much shorter timescale, *Schoof* [2010] showed how variations in
 121 surface melt influence ice velocity by driving rapid changes in the efficiency of subglacial
 122 drainage.

2. Model derivation

123 Here we develop a model for ice deformation near the locking point. We define the
 124 coordinate vector $\mathbf{x} = (x, y, z)$ so that x is parallel to the direction of ice stream flow, y
 125 is parallel to the bed and perpendicular to the ice stream margin, and z is the vertical
 126 height above the bed (see Figure 1). The transition from a deforming to an undeforming
 127 bed occurs across a semi-circular drainage channel centered on $y = z = 0$, with the ice
 128 stream located in $y < 0$ and the ridge located in $y > 0$. We define the velocity vector
 129 $\mathbf{u} = (u, v, w)$ such that u is the velocity in the x -direction, v the velocity in the y -direction,
 130 and w the velocity in the z -direction.

131 As is common when modeling flow in ice stream margins [*Jacobson and Raymond,*
 132 1998; *Schoof,* 2004, 2012; *Suckale et al.,* 2014; *Perol et al.,* 2015], we assume that all flow
 133 is in the downstream direction, making u the only non-zero component in the velocity
 134 vector, and that u is independent of x . These assumptions are justified by surface velocity

135 observations of ice streams showing that the downstream velocity is much greater than
 136 the lateral and vertical velocities v and w and that variations in u in the downstream
 137 direction are much smaller than variations in the lateral and vertical directions. The
 138 single non-zero component of the velocity vector $u(y, z)$ leads to just two non-zero shear
 139 strain rates,

$$\dot{\epsilon}_{xy} = \frac{1}{2} \frac{\partial u}{\partial y} \quad , \quad \dot{\epsilon}_{xz} = \frac{1}{2} \frac{\partial u}{\partial z}. \quad (1)$$

140 These lead to two non-zero shear stresses τ_{xy} and τ_{xz} , and the equations for mechanical
 141 equilibrium simplify to

$$\frac{\partial \tau_{xy}}{\partial y} + \frac{\partial \tau_{xz}}{\partial z} = 0, \quad (2)$$

142 describing a stress/deformation state called “anti-plane”. In the next section we show
 143 that the transition from a deforming to an undeforming bed concentrates large stresses
 144 at the locking point, with typical shear stresses of a few hundred kPa. Since these shear
 145 stresses are much greater than the gravitational driving stress for the ice stream, which is
 146 typically ~ 10 kPa, we can neglect the driving stress when solving for the stress field at
 147 the locking point using equation (2). However, as shown in Section 3, the gravitational
 148 driving stress still enters into our model by providing the far-field loading on the locking
 149 point, which is parameterized using a path-independent integral.

150 To close the model we need a rheological law linking strain rate and shear stress. Though
 151 ice can deform through a variety of mechanisms linked to physical phenomena such as dis-
 152 location motion and diffusion [*Schulson and Duval, 2009*], we assume a single deformation
 153 mechanism with a power law dependence,

$$\epsilon_{ij} = A \tau_E^{n-1} \tau_{ij}, \quad (3)$$

154 where $\tau_E = [\tau_{xy}^2 + \tau_{xz}^2]^{1/2}$ is the effective shear stress and $\epsilon_E = [\epsilon_{xy}^2 + \epsilon_{xz}^2]^{1/2}$ is the effective
 155 strain rate. Since the channel is expected to lie within the temperate ice zone [*Suckale*
 156 *et al.*, 2014; *Perol and Rice*, 2015], we assume for the local analysis of stressing near the
 157 channel that temperature, and hence A and n , are spatially uniform. In addition we
 158 neglect any dependence of A and n on melt fraction in the temperate ice, which may be
 159 a poor assumption for a channel with a well-developed englacial drainage system.

160 Equation (3) can model different deformation mechanisms by assuming different values
 161 of A and n . The majority of calculations in this paper assume a Glen's law rheology
 162 with $n = 3$ and $A = 2.4 \times 10^{-24} \text{ Pa}^{-3} \text{ s}^{-1}$, which are the values recommended in *Cuffey*
 163 *and Paterson* [2010] for $T = 0 \text{ }^\circ\text{C}$. However, *Goldsby and Kohlstedt* [2001] showed that
 164 Glen's original data plots on the boundary between two deformation mechanisms with
 165 stress exponents of 1.8 and 4, which may explain why Glen best fit his data with $n = 3$
 166 (see Figure 60.3 of *Goldsby* [2006].) Thus, we also model the dislocation creep rheology
 167 of *Durham et al.* [1997] using $n = 4$ and $A = 2.2 \times 10^{-30} \text{ Pa}^{-4} \text{ s}^{-1}$, which may dominate
 168 at the large shear stresses attained in the shear margin depending on exact values of
 169 temperature and grain size [*Goldsby*, 2006]. Finally, we produce some results using a
 170 Newtonian rheology with $n = 1$ and $A = 2.4 \times 10^{-14} \text{ Pa}^{-1} \text{ s}^{-1}$, where this value of A the
 171 effective viscosity predicted by Glen's law evaluated at 100 kPa (a typical shear stress in
 172 a shear margin).

3. Deformation around a sharp transition

173 As noted in *Suckale et al.* [2014], the deformation near the locking point is equivalent
 174 to an anti-plane shear crack in a creeping solid. Recognizing this correspondence, we use

175 methods from fracture mechanics to solve for the stress and velocity fields around a sharp
 176 transition from a deforming to an undeforming bed at $y = 0$.

177 Following *Rice* [1967] and *Rice* [1968b], Appendix A develops a solution for the stress
 178 field and velocity field around a sharp transition from a deforming to an undeforming bed.
 179 Note that the solution for the stress around a sharp transition was previously developed
 180 in *Suckale et al.* [2014] and used to benchmark numerical solutions for velocity and heat
 181 production in a shear margin, but the physical significance of the singular stress field and
 182 the implications for the mechanical structure of a shear margin were not emphasized. The
 183 shear stress component τ_{xz} on the undeforming bed ($z = 0$ and $y > 0$) is given by

$$\tau_{sharp} = \left(\frac{nJ_{tip}}{(n+1)A\pi y} \right)^{1/(n+1)}. \quad (4)$$

184 The far-field loading is linked to the stress at the locking point using the path-independent
 185 integral from *Suckale et al.* [2014], leading to

$$J_{tip} = \frac{4HA\tau_{lat}^{n+1}}{n+1}, \quad \tau_{lat} = \left(\rho_{ice}gS - \frac{\tau_{base}}{H} \right) \frac{W}{2}. \quad (5)$$

186 Here H is the ice thickness, W is the ice stream width, ρ_{ice} is the ice density, g is gravity,
 187 $S > 0$ is the slope in the downstream direction, and τ_{base} is the basal resistance provided
 188 by the deforming bed. A simple force balance for the ice stream shows that τ_{lat} is the
 189 average lateral drag supported by the shear margin. The path-independent integral in
 190 *Suckale et al.* [2014] is an extension of the J-type integrals first introduced for cracks
 191 in elastic solids by *Rice* [1968a], *Cherepanov* [1968] and *Bilby and Eshelby* [1968], later
 192 generalized to the nonlinear creep rheologies we consider (e.g. *Goldman and Hutchinson*
 193 [1975], *Landes and Begley* [1976], *Kubo et al.* [1979], *Ben Amar and Rice* [2002]), and
 194 previously applied to glaciers by *McMeeking and Johnson* [1986]. Inserting equation (5)

195 into equation (4) we find

$$\tau_{sharp} = \tau_{lat} \left(\frac{4Hn}{(n+1)^2\pi y} \right)^{1/(n+1)}. \quad (6)$$

196 The lateral stress supported by the shear margin is transmitted to the undeforming bed
 197 beneath the ridge such that the stress on the undeforming bed is directly proportional to
 198 the lateral drag supported by the shear margin. Note that equation (5) is only valid when
 199 the J-integral is evaluated using a constant basal resistance beneath the ice stream, though
 200 the solution can be easily extended to account for a spatially variable basal resistance.

201 Equation (6) has three distinctive features. First, the shear stress on the undeforming
 202 bed is singular with infinite shear stresses on the undeforming bed expected at the locking
 203 point. Second, the power of the singularity depends on the stress exponent n , with
 204 larger values of n corresponding to less severe singularities. Finally, larger values of τ_{lat}
 205 concentrate larger stresses on the undeforming bed. A singular stress field is obviously
 206 unphysical due to the finite yield strength of the bed. *Schoof* [2004] and *Perol et al.*
 207 [2015] avoided this problem by using a spatially variable shear strength profile at the bed
 208 to find non-singular solutions where the stress concentration vanishes. This is equivalent
 209 to solving for the transition from a deforming to an undeforming bed that satisfies $J_{tip} = 0$,
 210 which produces a continuous stress at the locking point. The solutions of *Schoof* [2004]
 211 and *Perol et al.* [2015] are analogous to the cohesive zone models commonly used in
 212 fracture mechanics to eliminate crack tip singularities by appealing to a zone of enhanced
 213 resistance near the crack tip [*Barenblatt*, 1959; *Dugdale*, 1960; *Bilby et al.*, 1963]. We take
 214 a different approach where J_{tip} is finite but the maximum stress on the bed is limited by
 215 the presence of a channel at the locking point. Our approach is analogous to crack blunting
 216 in fracture mechanics, which relies on the maximum stress at the crack tip decreasing as

217 the radius of curvature of the crack (or now notch) tip increases. Note that our crack
218 blunting mechanism for a finite value of J_{tip} is only valid if the locking point coincides
219 with a channel (if not the shear stress on the bed is singular for non-zero values of J_{tip}).
220 However, even if the locking point is not collocated with a channel, the presence of a
221 drainage channel can still select the location of the locking point by raising the yield
222 strength of the till over a broad zone within the shear margin, as shown in *Perol et al.*
223 [2015] who model the hydrology of transport and pore fluid suction development along
224 the interface.

225 To begin we show that all the information about the far-field loading is transmitted
226 to the locking point through J_{tip} alone. To do this we compare the analytic prediction
227 valid near the locking point (see Appendix A) with results from numerical simulations
228 generated using the finite element package COMSOL for the whole ice stream model that
229 couples temperature and deformation from *Perol et al.* [2015]. Since the analytic solution
230 has a fixed functional form with a single free parameter J_{tip} we should be able to match the
231 numerical solutions over a range of r and θ using a single value of J_{tip} . Figure 2 shows the
232 match between the analytic and numerical solutions by plotting the downstream velocity
233 as a function of θ at five different values of r , as well as the shear stress on the undeforming
234 bed. The specific value of J_{tip} used to plot the analytic solution is found by fitting to the
235 numerical solution for downstream velocity at $r = 5$ m and this value is used to plot the
236 downstream velocity profile at other values of r as well as the stress on the undeforming
237 bed. In Figure 2 one simulation is performed for a temperature independent rheology
238 and a second simulation for the full temperature dependent rheology given in *Perol et al.*
239 [2015]. Since the two solutions are in good agreement for all curves plotted in Figure 2,

240 our results demonstrate that the asymptotic solution presented in Appendix A provides
241 a good approximation to the full numerical solution for several tens of meters around the
242 locking point.

243 We can exploit the fact that the length scale over which the analytic and numerical
244 solutions agree is at least an order of magnitude greater than the estimates for channel
245 radius in *Perol et al.* [2015] by making an approximation analogous to the small-scale
246 yielding approximation commonly used in fracture mechanics when the process zone at
247 the crack tip is small enough that the entire body can be treated as an elastic solid in a
248 continuum model [*Rice*, 1967, 1968b]. The equivalent approximation in our model is that
249 the region over which the channel perturbs the stress field is contained entirely within the
250 zone of validity for the asymptotic solution at a sharp transition from a deforming to an
251 undeforming bed, and thus all knowledge of the far-field deformation is transmitted to
252 the channel through the asymptotic solution. Even though the entire ice is creeping in
253 our model, henceforth we follow the terminology used in fracture mechanics and refer to
254 our approach as making a small-scale yielding approximation. The small-scale yielding
255 approximation allows us to draw two important conclusions. First, it tells us that all
256 information about the far-field deformation is carried to the locking point through a single
257 parameter J_{tip} , which controls the magnitude of the stresses in the asymptotic solution
258 valid at the transition from a deforming to an undeforming bed. Thus, ice stream scale
259 parameters such as W and τ_{base} influence the stress at the locking point only through
260 J_{tip} , greatly reducing the number of independent parameters we must consider. Second,
261 the small-scale yielding approximation allows us to study the spatial variations in stress

262 around a channel at the locking point by imposing the asymptotic solution from Appendix
263 A as a boundary condition far from the channel.

4. Stress field around a channel

264 Next, we investigate how a channel with a radius R at the locking point alters the
265 shear stress resolved on the undeforming bed. Since we neglect to model the stress field
266 within the till and only solve for the stress field within the ice, the exact point within the
267 channel where the bed transitions from deforming to undeforming is unimportant. All
268 that matters is that the bed on one side of the channel is deforming and the bed on the
269 other side is undeforming. Within the channel the shear stress on the till is controlled
270 by turbulent flow of water, which is unlikely to be large enough to cause the till to yield
271 for typical effective pressures in the channel but may allow erosion of the till to occur. A
272 sketch of the geometry assumed in our calculation can be found in Figure 1. To begin, we
273 use a complex variable method to solve analytically for a Newtonian rheology, then use
274 numerical simulations to extend our analysis to a power law rheology.

275 As discussed in Section 3, from our analogy with fracture mechanics we expect the
276 presence of a channel to limit the maximum stress on the undeforming bed to a finite
277 value that decreases as the channel radius increases. Our goal in this section is to quantify
278 how the stress on the undeforming bed varies with parameters such as channel radius,
279 ice stream width, and the average basal resistance beneath the ice stream. The small-
280 scale yielding approximation justified in the previous section greatly reduces the number
281 of independent parameters that influence the stress on the undeforming bed. Ice stream
282 scale parameters such as W and τ_{base} influence the stress at the locking point only through
283 J_{tip} . The significant reduction in the number of independent parameters allows us to

284 use dimensional analysis to tightly constrain the functional form of the stress on the
 285 undeforming bed. We find that the stress on the bed is a function of J_{tip}/A , R , n , and
 286 y alone. There is a single way to combine these parameters to produce a quantity with
 287 units of stress, and thus the stress on the undeforming bed is equal to

$$\tau = \tau_{sharp}(R)h\left(\frac{y}{R}, n\right), \quad (7)$$

288 where τ_{sharp} is the singular solution for a sharp transition given in equation (4) and h is a
 289 function we must solve for. For all cases the maximum stress on the bed, which is where
 290 the undeforming bed is most likely to yield, occurs at the channel wall and is equal to

$$\tau_{max} = \chi\tau_{sharp}(R), \quad (8)$$

291 where $\chi = h(1, n)$ is a function of the stress exponent n alone. Thus, if we can determine
 292 how the parameter χ depends on the stress exponent n then equation (8) provides a
 293 completely general solution that allows us to predict the maximum shear stress on the
 294 undeforming bed for any set of parameter choices.

4.1. Newtonian rheology

295 For a Newtonian rheology we can make significant progress analytically. When $n = 1$
 296 the equation for mechanical equilibrium reduces to Laplace's equation,

$$\frac{\partial^2 u}{\partial r^2} + \frac{1}{r} \frac{\partial u}{\partial r} + \frac{1}{r^2} \frac{\partial^2 u}{\partial \theta^2} = 0, \quad (9)$$

297 where r and θ are polar coordinates centered on the origin. We solve equation (9) in
 298 $R < r < \infty$ with the no slip boundary condition on the undeforming bed,

$$u = 0 \quad \text{on} \quad \theta = 0, \quad R < r < \infty, \quad (10)$$

299 and the traction free boundary condition on the deforming bed,

$$\frac{\partial u}{\partial \theta} = 0 \quad \text{on} \quad \theta = \pi, \quad R < r < \infty. \quad (11)$$

300 An additional traction free boundary condition is applied on the channel wall,

$$\frac{\partial u}{\partial r} = 0 \quad \text{on} \quad r = R, \quad 0 < \theta < \pi. \quad (12)$$

301 Finally we assume that u approaches the solution for a sharp transition developed in
302 appendix A as $r \rightarrow \infty$, consistent with our small-scale yielding approximation.

303 Equations (9)-(12) are solved using complex variables in Appendix B, leading to the
304 shear stress on the undefining bed,

$$\tau_{xz} = \left(\frac{J_{tip}}{2A\pi y} \right)^{1/2} \left(1 + \frac{R}{y} \right). \quad (13)$$

305 We notice two distinctive features about this solution. First, the solution for a sharp
306 transition is the asymptotic limit of equation (4) when $y \gg R$. Thus, the presence of a
307 channel only alters the stress field on the bed in the immediate vicinity of the channel, and
308 far from the channel the stress field is the same as that predicted for a sharp transition.
309 Second, the presence of the channel caps the maximum shear stress on the bed at a finite
310 value,

$$\tau_{max} = \left(\frac{2J_{tip}}{A\pi R} \right)^{1/2}. \quad (14)$$

311 Note that a larger channel radius R leads to a lower maximum shear stress on the bed.

312 Comparing equation (14) to the solution for a sharp transition we find

$$\tau_{max} = 2\tau_{sharp}(R), \quad (15)$$

313 and thus $\chi = 2$ for $n = 1$. The maximum stress applied to the bed is equal to twice the
314 stress predicted by evaluating the singular solution for a sharp transition at the channel

315 radius R . As highlighted before, the finite maximum stress allows for a stable margin con-
 316 figuration where the stress on the undeforming bed is always less than the yield strength
 317 of the bed even when $J_{tip} \neq 0$.

4.2. Nonlinear rheology

318 The complex variable solution presented in the previous subsection cannot be gener-
 319 alized to a nonlinear rheology so we study other values of the stress exponent n using
 320 numerical solutions. We use a finite difference method on a uniform grid in r and θ and
 321 enforce the far-field velocity field given by equation (A24) on a semi-circular boundary
 322 with radius D . The traction free boundary condition on the channel wall remains the same
 323 as in the previous subsection and the boundary conditions on the bed are now applied
 324 for $R < r < D$. The finite domain size introduces an additional dimensionless param-
 325 eter R/D into equation (7), but we expect to recover the solution where the boundary
 326 conditions are applied at infinity as $R/D \rightarrow 0$.

327 The homogeneous boundary conditions allow us to calculate the dependence of χ on
 328 R/D analytically for $n = 1$. We find

$$\chi = 2 \left(1 + \frac{R}{D} \right)^{-1}. \quad (16)$$

329 As expected, $\chi \rightarrow 2$ as $R/D \rightarrow 0$. Next we determine how χ depends on R/D for several
 330 values of n numerically. Figure 3 shows how χ varies with R/D for $n = 1$, $n = 3$, and
 331 $n = 4$ when the channel radius is fixed at $R = 1$ m and the outer radius D is varied.
 332 To perform these simulations we assume an ice thickness of 1 km, an ice stream width of
 333 34 km, a slope $S = 0.0012$, and a basal stress of $\tau_{base} = 3.5$ kPa. These parameters are
 334 intended to model Dragon margin of Ice Stream B2 and are equivalent to $\tau_{lat} = 124$ kPa.

335 We observe a weak dependence of χ on R/D for all n , with larger values of R/D leading
 336 to smaller values of χ . Our analytic solution for $n = 1$ allows us to guess a functional
 337 form for this dependence,

$$\chi = \chi_{inf}(n) \left(1 + \frac{R}{D}\right)^{-\frac{1}{n}}, \quad (17)$$

338 which is shown by dashed curves in Figure 3. We infer best fitting values for χ_{inf} of 1.15
 339 for $n = 3$ and 1.09 for $n = 4$. The final form for the maximum stress on the bed is

$$\tau_{max} = \chi(n) \left(\frac{nJ_{tip}}{(n+1)A\pi R}\right)^{1/(n+1)}. \quad (18)$$

340 where $\chi(n)$ is set to the value inferred in Figure 3 as $R/D \rightarrow 0$ (i.e. χ_{inf}).

341 Numerical simulations also allow us to study the spatial variations in shear stress on the
 342 undeforming bed when a channel is present. Figure 4 shows the stress on the undeforming
 343 bed for $n = 1$ and $n = 3$ and the parameters in Table 1. As the stress exponent increases
 344 the maximum stress on the undeforming bed drops significantly, in excellent agreement
 345 with the behavior predicted for a sharp transition in equation (4) that showed a strong
 346 dependence of the singularity on the stress exponent. Our simulations show that for $n = 3$
 347 and $n = 4$ the stresses calculated numerically accounting for the channel are comparable
 348 to the predictions for a sharp transition for several tens of meters adjacent to the channel.

4.3. The importance of basal resistance

349 Up until now we have neglected the basal resistance beneath the ice stream when solving
 350 for the stress field around the locking point, arguing that τ_{base} is much smaller than the
 351 large stresses concentrated near the locking point. While this is true for values of the basal
 352 resistance inferred beneath the majority of an ice stream – typically 1 – 5 kPa [Kamb,
 353 2001] – it may not be true for the large basal resistance we expect to occur near a channel

354 [*Perol et al.*, 2015]. We can make some simple estimates analytically if we assume that
355 $n = 1$ and the basal resistance immediately adjacent to the channel takes a uniform value
356 τ_f , which is linked to but potentially much greater than τ_{base} . As shown in Appendix B,
357 the stress on the undeforming bed is

$$\tau_{xz} = \tau_f + \sqrt{\frac{J_{tip}}{2\pi Ay}} \left(1 + \sum_{n=1}^{\infty} C_n \left(\frac{R}{y} \right)^n \right), \quad (19)$$

358 where the constants C_n are given in equations (B18) and (B19). Figure 5 plots the stress
359 on the undeforming bed for different values of τ_f using the parameters in Tables 1 and
360 2. Our results show that for these parameter choices the dependence of maximum stress
361 on τ_f is not significant, with the maximum stress on the bed increasing by approximately
362 25% as τ_f varies by 600 kPa. To explore the dependence on τ_f for other parameter choices
363 we use equation (19) to calculate the maximum stress on the bed,

$$\tau_{max} = \left(1 + \frac{4}{\pi} \right) \tau_f + \sqrt{\frac{2J_{tip}}{\pi AR}}. \quad (20)$$

364 Comparing the magnitude of the two terms in equation (20) we conclude that for all values
365 of J_{tip} the maximum stress resolved on the bed increases with τ_f , and this increase can be
366 significant if τ_f is comparable to $\tau_{sharp}(R)$. Note that even when $J_{tip} = 0$ the maximum
367 shear stress on the undeforming bed exceeds the yield strength of the deforming bed.

368 Our analysis could be extended to account for a nonlinear rheology and a spatially
369 variable basal resistance on the deforming bed numerically. However, as discussed in
370 more detail in Section 7.1, the exact form of the spatial variations in basal resistance is
371 currently unclear, and is complicated by many additional processes not accounted for here
372 including the coupling between in-plane and anti-plane deformation, a change in boundary
373 conditions across the channel, and changes in channel geometry due to asymmetric creep

closure. If our conclusion that the importance of τ_f increases as τ_f approaches $\tau_{sharp}(R)$ holds for $n \neq 1$ then we expect basal resistance to become more important as the stress exponent increases because the maximum stress on the bed decreases with increasing n .

5. Basal yield strength adjacent to channel

Here we model the yield strength of the undeforming bed adjacent to the channel, which is governed by a Coulomb-plastic rheology controlled by the effective stress in the till and a friction coefficient

$$\tau_{yield} = f(\sigma_n - p), \quad (21)$$

where σ_n is the normal stress acting on the bed, p is the pore pressure, and f is the friction coefficient of the till.

To determine the effective stress of the bed we model a steady state channel following the approach from *Röthlisberger* [1972]. First, we use the Gauckler-Manning law for turbulent flow in a conduit to relate the water flux in the channel Q_w to the channel geometry through

$$\frac{Q_w}{A_{ch}} = \frac{R_h^{2/3} S^{1/2}}{n_m}, \quad (22)$$

where A_{ch} is the area of the channel, R_h is the hydraulic radius of the channel, and n_m is the Gauckler-Manning coefficient. For the semi-circular channel shown in Figure 1,

$$A_{ch} = \frac{\pi R^2}{2}, \quad R_h = \frac{R}{2(1 + 2/\pi)}. \quad (23)$$

Combining equations (22) and (23) we solve for the channel radius,

$$R = 2^{5/8} \left(\frac{n_m Q_w}{\pi S^{1/2}} \right)^{3/8} \left(1 + \frac{2}{\pi} \right)^{1/4}. \quad (24)$$

Note that for fixed values of n_m and S the channel radius is a function of the water flux alone, with larger water fluxes leading to a larger channel radius.

391 The heat generated by turbulent flow in the channel leads to melting at the channel wall
 392 [*Röthlisberger, 1972; Shreve, 1972*]. Using the rate at which water flowing in the channel
 393 converts gravitational potential energy into heat we calculate the rate at which melting
 394 expands the channel radius,

$$\dot{R}_{melt} = \frac{\rho_w g S Q_w}{\pi L \rho_{ice} R}, \quad (25)$$

395 where ρ_w is the density of water and L is the latent heat of fusion for ice. Melting at the
 396 channel interface is balanced by creep closure of the channel due to the ice overburden.
 397 For the power law rheology given in equation (3) we use the solution from *Nye [1953]* for
 398 creep closure of a circular channel to estimate the closure rate as,

$$\dot{R}_{creep} = \frac{AR(\sigma_o - p)^n}{n^n}, \quad (26)$$

399 where $\sigma_o = \rho_{ice} g H$ is the ice overburden pressure. A steady state size occurs when melting
 400 at the channel wall exactly balances creep closure. Setting (25) equal to (26) we find that
 401 the pore pressure in the channel is equal to

$$p = \sigma_o - n \left(\frac{\rho_w g S Q_w}{\pi A L \rho_{ice} R^2} \right)^{1/n}. \quad (27)$$

402 Note that the pore pressure decreases as the flux within the channel increases, and thus
 403 the till yield strength in the vicinity of the channel increases with Q_w .

Perol et al. [2015] showed that hydraulic diffusion equilibrates the pore pressure in the
 till with the pore pressure in the channel over the few tens of meters immediately adjacent
 to the channel. However, the presence of a channel alters the yield strength immediately
 adjacent to the channel by changing the normal stress resolved on the till. We can use
 the creep closure solution from *Nye [1953]* to determine the normal stress resolved on the

till adjacent to the channel,

$$\sigma_n = p + (\sigma_o - p) \left(1 + \frac{2-n}{n} \left(\frac{R}{y} \right)^{2/n} \right). \quad (28)$$

404 Combining equations (27) and (28) with the Coulomb-plastic rheology from equation (21)

405 we calculate the strength of undeforming bed to be

$$\tau_{yield} = f \left(\frac{\rho_w g S Q_w}{\pi A L \rho_{ice} R^2} \right)^{1/n} \left(n + (2-n) \left(\frac{R}{y} \right)^{2/n} \right). \quad (29)$$

406 Equation (29) predicts large changes in the yield strength of the undeforming bed in the

407 immediate vicinity of the channel, with the strength increasing near the channel for $n < 2$

408 but decreasing near the channel for $n > 2$. The yield strength at the channel wall, where

409 the highest shear stress is resolved on the bed, is

$$\tau_{yield} = 2f \left(\frac{\rho_w g S Q_w}{\pi A L \rho_{ice} R^2} \right)^{1/n}. \quad (30)$$

6. Stable margin configurations

410 To determine when the locking point can be stably collocated with a channel we compare

411 the maximum stress on the undeforming bed with the yield strength at the channel wall.

412 We focus on a Glen's law rheology but generalize our analysis to other stress exponents in

413 Appendix C. Assuming that the bed first yields at the channel wall, where the maximum

414 shear stress on the bed is greatest, we use equations (18) and (30) to write the condition

415 for a stable margin configuration as

$$\chi \left(\frac{3J_{tip}}{4\pi AR} \right)^{1/4} < 2f \left(\frac{\rho_w g S Q_w}{\pi A L \rho_{ice} R^2} \right)^{1/3}. \quad (31)$$

416 We rearrange the inequality to find that a stable margin configuration only occurs when

417 the channel radius is less than the critical locking radius

$$R_{lock} = \left(\frac{2f}{\chi} \right)^{12/5} \left(\frac{\rho_w g S Q_w}{\pi A L \rho_{ice}} \right)^{4/5} \left(\frac{4\pi A}{3J_{tip}} \right)^{3/5}. \quad (32)$$

418 Even though larger channels are more effective at limiting the maximum stress on the
 419 undeforming bed, we find that a stable margin configuration occurs if the channel radius
 420 is lower than a critical value because the dependence of till strength on channel size is
 421 more sensitive than the dependence of the maximum stress on channel size.

422 For fixed material properties and far-field loading the channel radius and the locking
 423 radius are functions of the water flux in the channel alone. Figure 6 plots R and R_{lock} as
 424 a function of Q_w for the parameters in Table 1 and a Glen's law rheology. At low water
 425 fluxes the channel radius is larger than the locking radius R_{lock} , and thus the margin
 426 configuration is not stable. However, R_{lock} increases faster with Q_w than R , leading to a
 427 stable margin configuration above a critical flux water flux.

428 Using our formulae for R and R_{lock} we solve for the critical water flux that must be
 429 exceeded for a stable margin to occur,

$$Q_{lock} = 2^{25/17} \left(\frac{n_m}{\pi S^{1/2}} \right)^{15/17} \left(1 + \frac{2}{\pi} \right)^{10/17} \left(\frac{\chi}{2f} \right)^{96/17} \left(\frac{\pi A L \rho_{ice}}{\rho_w g S Q_w} \right)^{32/17} \left(\frac{3J_{tip}}{4\pi A} \right)^{24/17}. \quad (33)$$

430 Figure 7 plots Q_{lock} as a function of A for different values of f and τ_{lat} . We choose this
 431 range of A based on the scatter in the experimentally measured values of A at 0 °C
 432 reported in *Cuffey and Paterson* [2010]. We observe a strong dependence of the critical
 433 water flux on A , with the smallest values of A leading to the smallest values of Q_{lock} .
 434 If based on the estimates in *Perol et al.* [2015] we assume that a typical water flux in a
 435 channel is approximately 0.1 m³/s then Figure 7 suggests that the locking point is not
 436 collocated with a channel at Dragon margin if the ice deforms with a Glen's law rheology.
 437 Choosing a single value for the water flux, which varies significantly in space and time, is
 438 somewhat unsatisfying and long-term we hope to incorporate our analysis into a model

439 for ice stream hydrology that will allow us to solve for the water flux in the channel
440 instead of just picking a value. However, developing and analyzing such a model is far
441 beyond the scope of this paper.

442 We observe a strong dependence of Q_{lock} on τ_{lat} for all three stress exponents, as shown
443 in Figure 8. If we again choose a typical channel flux to be $0.1 \text{ m}^3/\text{s}$ then for a Glen's law
444 rheology the locking point can coincide with a channel if the lateral stress is less than ~ 50
445 kPa and for dislocation creep the locking point can coincide with a channel if the lateral
446 stress is less than ~ 115 kPa. Using data for a range of shear margins from *Joughin et al.*
447 [2002], *Perol and Rice* [2015] estimated that $\tau_{lat} \approx 100 - 135$ kPa. From these observations
448 we conclude that there are some scenarios where the locking point can be collocated with
449 a drainage channel, though this configuration is not probably typical and only occurs in
450 regions of high water flux. Predicting specific locations where the drainage channel is
451 likely collocated with a drainage channel is difficult due to the poor constraints on the
452 presence of drainage channels within shear margins and the water fluxes through such a
453 channel. Note that our results are sensitive to the assumed rheology, and collocation of
454 the locking point with a channel can only occur if the ice deformation at the locking point
455 follows the dislocation creep rheology of *Durham et al.* [1997], which dominates at the
456 highest shear stresses. Our results highlight the importance of properly determining how
457 ice deforms over a range of shear stresses, grain sizes, and temperatures.

7. Discussion

458 In this paper we investigated when the locking point can be collocated with a drainage
459 channel within a shear margin. We showed that the presence of the channel limits the
460 maximum shear stress on the undeforming bed and alters the yield strength of the till by

461 changing the normal stress on the ice-till interface. By determining when the shear stress
462 on the undeforming bed is always less than the till strength we found that the locking
463 point can be collocated with a drainage channel only if the water flux in the channel
464 exceeds a critical flux that depends sensitively on the ice rheology.

465 Our analysis complements *Perol et al.* [2015], which demonstrated how a drainage chan-
466 nel not collocated with the locking point can select the margin location by raising the yield
467 strength of the till over a broad zone within the shear margin. In contrast, our analysis
468 studied the scenario where the locking point is collocated with a channel and focused on
469 understanding how the presence of a channel alters the shear stress and normal stress
470 resolved on the undeforming bed. However, our conclusions are in good agreement with
471 *Perol et al.* [2015]. Figure 8 shows that for the Glen’s law rheology (i.e. $n = 3$) used
472 exclusively in *Perol et al.* [2015] the locking point cannot be collocated with a channel,
473 which is the same conclusion reached in *Perol et al.* [2015].

474 The two distinct hydrologic mechanisms presented in this paper and *Perol et al.* [2015]
475 – one with the locking point collocated with the channel and the other with the locking
476 point occurring inboard of the channel on a temperate bed – both become more effective
477 as the flux in the channel increases. Thus, the hydrologic mechanisms are most likely
478 to select the shear margin location in regions of high water flux. When the hydrologic
479 mechanisms are ineffective we expect the margin location to be controlled by where the
480 subglacial till freezes, a scenario studied in *Jacobson and Raymond* [1998], *Schoof* [2012],
481 and *Haseloff* [2015].

7.1. Limitations of model

482 In this subsection we outline the limitations of our model and discuss how these lim-
483 itation may alter our conclusions. The solution from *Nye* [1953] used to model creep
484 closure of the channel was developed for axisymmetric creep closure of a circular hole and
485 implicitly assumes free slip boundary conditions at the bed. However, our boundary con-
486 ditions are no slip on one side of the channel and a deforming bed providing a finite basal
487 resistance on the other. *Weertman* [1972] suggested that the change to no slip bound-
488 ary conditions at the bed will alter the strength of the undeforming bed in several ways.
489 First, additional basal resistance will lower the creep closure rate, leading to a lower pore
490 pressure in the channel and thus a stronger bed. If the realistic boundary conditions lead
491 to a creep closure rate equal to half the value predicted by equation (26) then the effective
492 stress in the channel increases by a factor of 2^n , which highlights the importance of ac-
493 curately determining n . Second, *Weertman* [1972] showed that for a Newtonian rheology
494 the no slip boundary condition reduces the normal stress applied to the bed, and thus the
495 yield strength of the till, far from the channel. However, *Weertman* [1972] was unable to
496 produce a formula for the normal stress immediately adjacent to the channel or account
497 for a spatially variable in-plane strain rate and a nonlinear rheology. Finally, our creep
498 closure model neglects to couple the in-plane strain rates from channel closure with the
499 large anti-plane strain rates present at the locking point. This important coupling, first
500 noted in *Röthlisberger* [1972] and studied further in *Weertman* [1972] and *Fernandes et al.*
501 [2014], is expected to lead to easier channel closure, and thus a lower effective stress and
502 yield strength adjacent to the channel. Currently it is unclear how the three uncertainties
503 associated with the closure model, one of which raises τ_{yield} and two of which lower τ_{yield} ,
504 balance each other to control the yield strength of the till near a drainage channel. Note

505 that the coupling with lateral flow in our model through the nonlinear ice rheology is
506 physically different from the dependence on lateral flow in *Suckale et al.* [2014], which
507 highlighted that the advection of cold ice into the margin driven by lateral gradients in
508 ice thickness greatly influences the large scale temperature structure of a shear margin. In
509 our model we consider a channel sitting within a broad region of temperate ice, and thus
510 temperature gradients are unimportant and we are insensitive to the effects of advection.

511 Determining how the presence of a channel alters the till yield strength is important
512 for the deforming bed as well as the undeforming bed. As shown in Section 4.3, the
513 basal resistance provided by the deforming bed near the channel plays an important role
514 in setting the maximum stress on the undeforming bed. However, we did not explore
515 this effect in depth because the exact functional form of the basal resistance is unclear.
516 To clarify the spatial variations in basal resistance on the deforming bed requires new
517 calculations accounting for realistic basal boundary conditions and the coupling between
518 in-plane and anti-plane deformation, as discussed earlier in this section. Note that a broad
519 zone of elevated basal resistance will lower J_{tip} , as shown in *Perol et al.* [2015], leading to
520 a substantially lower value of Q_{lock} and a greater likelihood that the locking point could
521 be collocated with a drainage channel.

522 Next we discuss our assumed channel geometry. The asymmetry of the boundary con-
523 ditions across the channel will lead to asymmetric creep closure of the channel, suggesting
524 that our assumption of a semi-circular may not be valid. If creep closure is less rapid near
525 the undeforming bed then the radius of curvature of the channel wall at the undeforming
526 bed may be greater than the average channel radius, making the stress limiting effects of
527 the channel more effective. Note that the asymmetry of the boundary conditions will lead

528 to different normal stresses on the deforming and undeforming bed, leading to a jump in
529 the till yield strength across the channel. Furthermore, asymmetry in the creep closure of
530 the channel will lead to gradual migration of the channel towards the undeforming bed.
531 The upper bound for this migration rate is the melt rate at the channel wall, which rarely
532 exceeds 0.1 m/a in our calculations.

533 Another limitation of the model regards the details of how the subglacial till deforms.
534 For simplicity we assume a deforming bed on one side of the channel and an undeforming
535 bed on other, but do not explicitly model how this transition occurs in the till. Fur-
536 thermore, we assume that the entirety of the channel is incised into the ice, ignoring the
537 possibility that a channel may develop in the till or other physical effects that may become
538 important at high effective stresses such as the penetration of ice into the till studied in
539 *Rempel* [2009]. If the radius of curvature at the channel wall is lowered by incision into
540 the till then our mechanism for limiting the maximum stress using a channel becomes less
541 effective.

542 Finally our model could be extended to account for non-steady state effects such as vari-
543 able water flux, time-dependent transport of water to the channel, and evolving channel
544 shape. Non-steady state effects could be particularly important when determining how
545 our results relate to observations of margin migration.

7.2. Importance of ice rheology

546 While a simple Glen's law rheology may be a good approximation for ice stream scale
547 simulations, our paper highlights the importance of properly determining the dominant
548 physical processes that allow ice to deform over a range of stresses. Figures 7 and 8
549 show that the critical water flux that controls if the transition from a deforming to an

550 undeforming bed across a channel is stable depends sensitively on the assumed values of
551 n and A . More generally, the closure rate of and pore pressure in a channel, important
552 considerations in all models of subglacial drainage channels, depend strongly on A and n .

553 The high shear stresses present at the locking point may allow deformation to occur
554 solely through dislocation creep. Dislocation creep is the dominant deformation mecha-
555 nism ice at the highest shear stresses and is governed by $n = 4$ [Durham *et al.*, 1997]. If
556 we assume a grain size of 4 mm – a typical grain size observed in the shear margin cores
557 from Jackson and Kamb [1997] – Figure 60.3 from Goldsby [2006] predicts that disloca-
558 tion creep dominates for stresses exceeding ~ 200 kPa. Figure 4 shows that this critical
559 stress is lower than the shear stress expected on the undeforming bed for a channel with
560 radius 1 m, and thus $n = 4$. However, the stress concentration at the locking point could
561 drive significant grain size reduction. If the grain size is reduced to 1 mm then dislocation
562 creep dominates above ~ 1 MPa, and if the grain size reaches $100 \mu\text{m}$ then dislocation
563 creep dominates above ~ 2 MPa. For comparison, Perol *et al.* [2015] and Figure 4 show
564 that peak stresses within the shear margin are at least a few hundred kPa, though it
565 should be noted that the analysis in Perol *et al.* [2015] uses a Glen’s law rheology with the
566 temperature dependence from Cuffey and Paterson [2010]. If dislocation creep is not the
567 dominant deformation mechanism then the grain-boundary sliding regime governed by
568 $n = 1.8$ described in Goldsby and Kohlstedt [2001] dominates. The concentrated stresses
569 present at the locking point may produce a fabric in the ice. If this occurs then the value
570 of A governing the creep closure of the channel will differ from the value of A governing
571 the shear stress resolved on the bed.

572 In Section 2 we assumed that the melt content of the ice immediately adjacent to the
573 channel could be neglected when determining values of A and n . However, this assumption
574 may not be valid for all shear margins, especially if a large quantity of melt is generated
575 in the temperate ice. Accurately determining the effect of melt fraction on rheology is
576 beyond the capability of current experiments, though the experiments in *Duval* [1977] and
577 *Lliboutry and Duval* [1985] showed that a melt fraction of just 1.1% increases A by about a
578 factor of three. Other experiments performed on partially molten olivine – which deforms
579 through similar physical mechanisms as ice – showed increasing the melt fraction promotes
580 grain boundary diffusion creep, which is governed by $n = 1$ [*Cooper and Kohlstedt*, 1986].
581 Thus, it may not be sufficient to just make A a function of the melt fraction, and there
582 may also be a change in n at a given shear stress.

583 When predicting the melt content in the ice adjacent to the channel it may be helpful
584 to consider two end-members dictated by the balance between subglacial drainage and
585 englacial drainage. For the case where the subglacial transport of melt – either through
586 the till or along the ice-till interface – is more efficient than englacial transport we expect
587 melt to be routed to the bed before flowing to the channel. For this scenario we expect the
588 water content in the temperate ice immediately adjacent to the channel to be negligible. In
589 contrast, if subglacial flow is inefficient then melt may be routed to the channel englacially,
590 implying a significant water content in the ice next to the channel, and thus a much
591 larger value of A . Our qualitative argument assuming that drainage naturally selects
592 the most efficient route from where melt is generated to the channel is motivated by the
593 quantitative analysis in *Fisher* [1951] that studied how diffusion along grain boundaries
594 and diffusion through individual crystals balance to control diffusion into a polycrystalline

595 metal. *Fisher* [1951] showed that if the grain boundary diffusivity is significantly higher
596 than the diffusivity for an individual crystal then the most efficient way to penetrate into
597 the polycrystal is to diffuse as far as possible along the grain boundary before leaking into
598 the adjoining crystal. In this analogy subglacial drainage is equivalent to diffusion along
599 a grain boundary and englacial drainage is equivalent to diffusion through an individual
600 crystal.

8. Conclusions

601 Our paper investigated when the transition from a deforming to an undeforming bed
602 can occur across a subglacial drainage channel. We showed that the presence of a channel
603 at the locking point limits the maximum shear stress resolved on the undeforming bed and
604 alters the till strength by changing the normal stress on the ice-till interface. Comparing
605 stress and strength on the undeforming bed, we determined that the locking point can
606 be collocated with a drainage channel if and only if the water flux in the channel exceeds
607 a critical value. For a Glen's law rheology this critical flux is unrealistically large if the
608 average lateral shear stress in the shear margin exceeds $\sim 35 - 50$ kPa. However, for the
609 dislocation creep rheology of *Durham et al.* [1997] the critical flux is substantially lower,
610 and the locking point can be collocated with the channel if the average lateral shear stress
611 in the shear margin is less than $\sim 85 - 115$ kPa. From these observations we conclude
612 that there are some scenarios where the locking point can be collocated with a drainage
613 channel, though this configuration is probably not typical.

614 **Acknowledgments.** This research was supported by the National Science Foundation
615 through the Office of Polar Programs award number 1341499 (March 2014 to February

616 2017), and previously grant ANT-0739444 (June 2008 to May 2012) to Harvard University.

617 Input files used for the numerical simulations are available upon request by emailing the

618 corresponding author at jplatt@dtm.ciw.edu The authors thank Christian Schoof, Tim

619 Creyts and Alan Rempel for fruitful discussions.

Appendix A: Derivation of near-tip solution

In this appendix we solve for the stress field and velocity near the transition from a
 deforming to an undeforming bed, assuming a sharp transition at $y = z = 0$. We use the
 hodograph plane methods from *Rice* [1967] and *Rice* [1968b] to solve for the downstream
 velocity profile as well as the stress field. Our approach is different from *Suckale et al.*
 [2014] because we need to solve for the downstream velocity profile, as well as the stress
 field. The downstream velocity profile is later used as a boundary condition in numerical
 simulations for the stress field around a channel.

To begin we define the Legendre transform of the downstream velocity u

$$\psi = y\dot{\gamma}_y + z\dot{\gamma}_z - u, \quad (\text{A1})$$

where $\dot{\gamma}_y$ and $\dot{\gamma}_z$ are the engineering strain rates defined by

$$\dot{\gamma}_y = \frac{\partial u}{\partial y}, \quad \dot{\gamma}_z = \frac{\partial u}{\partial z}. \quad (\text{A2})$$

The effective engineering strain rate is equal to $[\dot{\gamma}_y^2 + \dot{\gamma}_z^2]^{1/2}$, and the power law rheology
 given in equation (3) can be written as $\dot{\gamma} = 2A\tau^n$. Differentiating equation (A1) with
 respect to $\dot{\gamma}_y$ and $\dot{\gamma}_z$, and noting that

$$\frac{\partial u}{\partial \dot{\gamma}_y} = \dot{\gamma}_y \frac{\partial y}{\partial \dot{\gamma}_y} + \dot{\gamma}_z \frac{\partial z}{\partial \dot{\gamma}_y}, \quad \frac{\partial u}{\partial \dot{\gamma}_z} = \dot{\gamma}_y \frac{\partial y}{\partial \dot{\gamma}_z} + \dot{\gamma}_z \frac{\partial z}{\partial \dot{\gamma}_z}, \quad (\text{A3})$$

we can relate the first derivatives of ψ to the coordinates y and z through

$$\frac{\partial \psi}{\partial \dot{\gamma}_y} = y, \quad \frac{\partial \psi}{\partial \dot{\gamma}_z} = z. \quad (\text{A4})$$

Following *Rice* [1967] we rewrite the equation for mechanical equilibrium as

$$\frac{\partial y}{\partial \tau_{xy}} + \frac{\partial z}{\partial \tau_{xz}} = 0 \quad (\text{A5})$$

634 and define polar coordinates in the strain plane

$$\dot{\gamma}_y = -\dot{\gamma} \sin \phi \quad , \quad \dot{\gamma}_z = \dot{\gamma} \cos \phi. \quad (\text{A6})$$

635 Note that in the hodograph plane radius from the origin is equal to the equivalent engi-
636 neering strain rate $\dot{\gamma}$. As shown in *Rice* [1967], the equation for mechanical equilibrium
637 in the hodograph plane is

$$n \frac{\partial^2 \psi}{\partial \dot{\gamma}^2} + \frac{1}{\dot{\gamma}} \frac{\partial \psi}{\partial \dot{\gamma}} + \frac{1}{\dot{\gamma}^2} \frac{\partial^2 \psi}{\partial \phi^2} = 0. \quad (\text{A7})$$

638 Note that transforming from the physical plane to the hodograph plane has turned the
639 nonlinear equation for u into a linear equation for ψ .

640 Next we map the two boundary conditions in the physical plane to the hodograph plane.

641 We can determine where these two boundary conditions map to in the hodograph plane
642 by noting that for the traction free condition $\dot{\gamma}_z = 0$ and $\dot{\gamma}_y < 0$, while for the no slip
643 boundary condition $\dot{\gamma}_y = 0$ and $\dot{\gamma}_z > 0$. Thus the no-slip condition maps to the positive
644 $\dot{\gamma}_z$ -axis and the traction free condition maps to the negative $\dot{\gamma}_y$ -axis.

645 Having located the boundary conditions in the hodograph plane we next determine the
646 form of the boundary conditions. For the no slip condition all three terms in equation
647 (A1) vanish, leading to

$$\psi = 0 \quad \text{on} \quad \phi = 0. \quad (\text{A8})$$

648 In the physical plane the traction free boundary condition occurs on $z = 0$, and thus from
649 equation (A4) we find $\partial \psi / \partial \dot{\gamma}_z = 0$. This is equivalent to saying that the normal derivative
650 must vanish,

$$\frac{\partial \psi}{\partial \phi} = 0 \quad \text{on} \quad \phi = \pi/2. \quad (\text{A9})$$

651 Figure 9 shows a sketch of the physical plane and hodograph highlighting the equations
 652 and boundary conditions.

653 We solve equation (A7) with the boundary conditions given in (A8) and (A9) using the
 654 separable solution

$$\psi = -C\dot{\gamma}^{-1/n} \sin \phi, \tag{A10}$$

655 where the constant $C > 0$ is an arbitrary constant that we determine later and the negative
 656 sign is required to ensure that when we map back to the physical plane our solution lies in
 657 $z > 0$. Note that equation (A10) is a much simplified case of the eigenfunction expansion
 658 given in the original solution of this problem from *Rice* [1967]. Using the solution for
 659 ψ we now determine the mapping to switch between $(\dot{\gamma}, \phi)$ and (r, θ) . In the hodograph
 660 plane polar coordinates defined in equation (A6) equation (A4) becomes

$$y = -\sin \phi \frac{\partial \psi}{\partial \dot{\gamma}} - \frac{\cos \phi}{\dot{\gamma}} \frac{\partial \psi}{\partial \phi}, \tag{A11}$$

661

$$z = \cos \phi \frac{\partial \psi}{\partial \dot{\gamma}} - \frac{\sin \phi}{\dot{\gamma}} \frac{\partial \psi}{\partial \phi}. \tag{A12}$$

662 Inserting the solution given in equation (A10) we find

$$y = -C\dot{\gamma}^{-(n+1)/n} \left(\left(\frac{n+1}{n} \right) \sin^2 \phi - 1 \right), \tag{A13}$$

663

$$z = \frac{n+1}{n} C\dot{\gamma}^{-(n+1)/n} \sin \phi \cos \phi. \tag{A14}$$

664 Dividing z by y we arrive at an equation for θ ,

$$\tan \theta = \frac{(n+1) \tan \phi}{n - \tan^2 \phi}. \tag{A15}$$

665 Noting that equation (A15) defines a quadratic equation in $\tan \phi$ we solve to find

$$\tan \phi = -\frac{(n+1) \cot \theta}{2} + \sqrt{\frac{(n+1)^2 \cot^2 \theta}{4} + n}. \tag{A16}$$

666 To find the radius r in the physical plane we use $r^2 = y^2 + z^2$, leading to

$$r = C\dot{\gamma}^{-(n+1)/n} \sqrt{\left(\frac{1+n}{n}\right) \left(\frac{1-n}{n}\right) \sin^2 \phi + 1}. \quad (\text{A17})$$

667 We rearrange equation (A17) to give $\dot{\gamma}$ in terms of r ,

$$\dot{\gamma}^{(n+1)/n} = \frac{C}{r} \sqrt{\left(\frac{1+n}{n}\right) \left(\frac{1-n}{n}\right) \sin^2 \phi + 1}, \quad (\text{A18})$$

668 where $\tan \phi$ is given by equation (A16) and we use the trigonometric identity,

$$\sin^2 \phi = \frac{\tan^2 \phi}{1 + \tan^2 \phi}. \quad (\text{A19})$$

669 At this point we solve for the constant C using the J-integral, which links the far-field
670 loading to the asymptotic solution valid near the locking point. This process is greatly
671 simplified by comparing with the solution for the stress field around a sharp transition
672 from *Suckale et al.* [2014]. Comparing our solution for z given in equation (A12) with
673 equation (B2) in *Suckale et al.* [2014] allows us to relate the function F defined in *Suckale*
674 *et al.* [2014] to our solution through

$$F = \frac{n+1}{2n} C \dot{\gamma}^{-(n+1)/n}. \quad (\text{A20})$$

675 Using the definition of F given in equation (B4) of *Suckale et al.* [2014] we arrive at

$$C = \frac{2n(2A)^{1/n} J_{tip}}{\pi(n+1)}. \quad (\text{A21})$$

676 Determining the constant C completes our solution for ψ .

677 Finally we invert for u using

$$u = \dot{\gamma} \frac{\partial \psi}{\partial \dot{\gamma}} - \psi, \quad (\text{A22})$$

678 allowing us to find the velocity field around the locking point in terms of $\dot{\gamma}$ and ϕ ,

$$u = \frac{(n+1)C}{n} \dot{\gamma}^{-1/n} \sin \phi. \quad (\text{A23})$$

679 Using equations (A16) and (A18) we rewrite this in terms of r and θ to find,

$$u = \left(\frac{2A(n+1)}{n} \right)^{1/(n+1)} \left(\frac{2J_{tip}}{\pi} \right)^{n/(n+1)} r^{1/(n+1)} g(\theta), \quad (\text{A24})$$

680 where the shape of the velocity field is given by the function

$$g(\theta) = \left(\frac{n^2 f^{n+1}}{(n^2 + f)(1 + f)^n} \right)^{1/(2n+2)} \quad (\text{A25})$$

681 and the function $f(\theta)$ is

$$f(\theta) = n + \frac{(n+1)^2}{2} \cot^2 \theta - (n+1) \cot \theta \sqrt{\frac{(n+1)^2}{4} \cot^2 \theta + n}. \quad (\text{A26})$$

682 Noting that $\partial u / \partial y = 0$ on the undeforming bed, we inserting the derivative of u with
 683 respect to z into the power law given in equation (3) to find the stress on the undeforming
 684 bed,

$$\tau_{sharp} = \left(\frac{nJ_{tip}}{(n+1)A\pi y} \right)^{1/(n+1)}. \quad (\text{A27})$$

Appendix B: Solution for circular channel and Newtonian rheology

685 Here we develop an analytic solution for the stress on the undeforming bed a semi-
 686 circular channel in ice with a Newtonian rheology. Because our solution relies on complex
 687 variables, it cannot be extended to other stress exponents $n \neq 1$. To begin we assume that
 688 the basal resistance acting on the deforming bed is much smaller than the concentrated
 689 stresses at the locking point, allowing us to model the deforming bed as a stress free
 690 boundary. After we generalize the solution to account for the finite basal resistance that
 691 *Perol et al.* [2015] argued is important to a drainage channel in the margin

B1. Negligible basal resistance

692 To begin we define the complex coordinate $\xi = y + iz = re^{i\theta}$ and the holomorphic
 693 function G such that

$$u = 2A\Im(G(\xi)), \quad (\text{B1})$$

694 where $\Im(G)$ indicates the imaginary part of G . Differentiating G with respect to ξ we
 695 find

$$G'(\xi) = \tau_{xz} + i\tau_{xy}. \quad (\text{B2})$$

696 Based on the small-scale yielding assumption validated in Section 3, we require that G
 697 match the solution for a sharp transition as $\xi \rightarrow \infty$,

$$G'(\xi) \rightarrow \left(\frac{J_{tip}}{2A\pi}\right)^{1/2} \xi^{-1/2} \quad \text{as } \xi \rightarrow \infty. \quad (\text{B3})$$

698 In addition we have a traction free boundary condition at the channel face $r = R$,

$$\tau_{zy}n_y + \tau_{xz}n_z = 0, \quad (\text{B4})$$

699 where n_y and n_z are the y and z components of the unit normal to the channel wall
 700 respectively. Using our definition of ξ and equation (B2) we rewrite the traction free
 701 condition on the channel face as

$$\Im[e^{i\theta}G'(\xi)] = 0. \quad (\text{B5})$$

702 To match the stress free boundary condition at $r = R$ we look for a series solution,

$$G'(\xi) = \left(\frac{J_{tip}}{2A\pi}\right)^{1/2} \xi^{-1/2} \left(1 + \sum_{k=1}^{\infty} \frac{C_k}{\xi^k}\right), \quad (\text{B6})$$

703 using the fact that all holomorphic functions are analytic to write $G'(\xi)$ as a series expan-
 704 sion in ξ . Our series expansion naturally satisfies the no slip condition at $\theta = 0$ and the

705 traction free boundary condition at $\theta = \pi$. Inserting (B6) into (B5) leads to

$$\Im \left[e^{i\theta/2} \left(1 + \sum_{k=1}^{\infty} C_k R^{-k} e^{-ik\theta} \right) \right] = 0, \quad (\text{B7})$$

706 which is satisfied by setting $C_1 = R$ and $C_k = 0$ for $k > 1$. Thus, our final solution for

707 $G'(\xi)$ is

$$G'(\xi) = \left(\frac{J_{tip}}{2A\pi} \right)^{1/2} \xi^{-1/2} \left(1 + \frac{R}{\xi} \right). \quad (\text{B8})$$

708 We extract the shear stress along the undeforming portion of the bed by setting $\xi = y$ to

709 arrive at

$$\tau_{xz} = \left(\frac{J_{tip}}{2A\pi y} \right)^{1/2} \left(1 + \frac{R}{y} \right). \quad (\text{B9})$$

B2. Finite basal resistance

710 The method used to calculate the maximum stress on the locked portion of the bed for

711 a Newtonian rheology and a circular channel can be generalized to allow for a non-zero

712 basal stress. When the deforming bed applies a non-zero shear stress τ_f to the ice the

713 far-field solution for a singular crack becomes

$$\tau_{xz} + i\tau_{xy} = \tau_f + \left(\frac{J_{tip}}{2A\pi} \right)^{1/2} \xi^{-1/2}, \quad (\text{B10})$$

714 which is equal to the linear superposition of a constant stress field $(\tau_{xy}, \tau_{xz}) = (0, \tau_f)$ and

715 the solution for a sharp transition assuming that the bed provides no resistance. To find a

716 solution that approaches the singular solution as $\xi \rightarrow \infty$ we again use a series expansion,

$$\tau_{xz} + i\tau_{xy} = \tau_f + \left(\frac{J_{tip}}{2A\pi} \right)^{1/2} \xi^{-1/2} \left(1 + \sum_{k=1}^{\infty} \frac{C_k}{\xi^k} \right). \quad (\text{B11})$$

717 Inserting this expansion into the traction free boundary condition given in equation (B5)

718 we arrive at

$$\tau_f \sin \theta + \sqrt{\frac{J_{tip}}{2\pi AR}} \sum_{k=0}^{\infty} C_k \sin((1/2 - n)\theta) = 0, \quad (\text{B12})$$

719 where we have set $C_0 = 1$. To find the coefficients C_k we use the series expansion

$$\sin \theta = \sum_{k=1}^{\infty} D_k \sin((n-1/2)\theta) \quad , \quad -\pi \leq \theta < \pi, \quad (\text{B13})$$

720 which is equivalent to

$$\sin 2\psi = \sum_{k=1,3,5,\dots}^{\infty} D_k \sin(n\psi) \quad , \quad -\frac{\pi}{2} \leq \psi < \frac{\pi}{2}. \quad (\text{B14})$$

721 To find the coefficients D_k we use the orthogonality condition

$$\int_{-\pi/2}^{\pi/2} \sin(n\psi) \sin(m\psi) d\psi = \frac{\pi}{2} \delta_{mn}, \quad (\text{B15})$$

722 where δ_{mn} is the Kronecker delta and m, n are both odd. Using equation (B15) we

723 calculate the formula for D_k ,

$$D_k = \frac{2}{\pi} \int_{-\pi/2}^{\pi/2} \sin(2\psi) \sin(k\psi) d\psi, \quad (\text{B16})$$

724 and evaluate this to find

$$D_k = \frac{8}{\pi(k^2 - 4)} (-1)^{\frac{(k+1)}{2}}. \quad (\text{B17})$$

725 Having found the values for D_k we can convert this to the coefficients C_k . We find that

$$C_1 = 1 + \frac{8\tau_f}{3\pi} \sqrt{\frac{2\pi AR}{J_{tip}}}, \quad (\text{B18})$$

726

$$C_n = \sqrt{\frac{2\pi AR}{J_{tip}}} \frac{8\tau_f}{\pi(2n+1)(2n-3)} (-1)^n \quad , \quad n \geq 2. \quad (\text{B19})$$

727 These coefficients allow us to calculate the stress applied to the locked portion of the bed

$$\tau_{xz} = \tau_f + \sqrt{\frac{J_{tip}}{2\pi Ay}} \left(1 + \sum_{n=1}^{\infty} C_n \left(\frac{R}{y} \right)^n \right). \quad (\text{B20})$$

Appendix C: Generalization of locking to radius to $n \neq 3$

728 Here we generalize the analysis in section 6 to stress exponents $n \neq 3$. To do this we

729 compare the maximum stress on the bed given by equation (18),

D R A F T

May 12, 2016, 4:11pm
 $\chi \left(\frac{n J_{tip}}{(n+1)\pi AR} \right)^{\frac{1}{n+1}}$

D R A F T

(C1)

730 with the yield strength of the undeforming bed adjacent to the channel from equation
731 (30),

$$2f \left(\frac{\rho_w g S Q_w}{\pi L \rho_{ice} A R^2} \right)^{1/n}. \quad (C2)$$

732 Setting the stress less than or equal to the yield strength of the undeforming lead to the
733 inequality,

$$\chi \left(\frac{n J_{tip}}{(n+1)\pi A R} \right)^{1/(n+1)} < 2f \left(\frac{\rho_w g S Q_w}{\pi L \rho_{ice} A R^2} \right)^{1/n}. \quad (C3)$$

734 We rearrange to find the critical locking radius below which a stable margin configuration
735 occurs,

$$R < R_{lock}, \quad (C4)$$

736 where the locking radius is defined as

$$R_{lock} = \left(\frac{2f}{\chi} \right)^{\frac{n(n+1)}{n+2}} \left(\frac{\rho_w g S Q_w}{\pi L \rho_{ice} A} \right)^{\frac{n+1}{n+2}} \left(\frac{\pi A (n+1)}{n J_{tip}} \right)^{\frac{n}{n+2}}. \quad (C5)$$

737 Recalling that for fixed material properties and loading conditions R and R_{lock} depend on
738 the water flux Q_w alone, we rewrite the inequality (C5) as

$$Q_w > Q_{lock}, \quad (C6)$$

739 where the critical water flux that must be exceeded for locking to occur is

$$Q_{lock} = 2^{\frac{5(n+2)}{5n+2}} \left(\frac{n_m}{\pi S^{1/2}} \right)^{\frac{3(n+2)}{5n+2}} \left(1 + \frac{2}{\pi} \right)^{\frac{2(n+2)}{5n+2}} \left(\frac{\chi}{2f} \right)^{\frac{8n(n+1)}{n+2}} \left(\frac{\pi L \rho_{ice} A}{\rho_w g S} \right)^{\frac{8(n+1)}{5n+2}} \left(\frac{n J_{tip}}{\pi A (n+1)} \right)^{\frac{8n}{5n+2}}. \quad (C7)$$

References

- 740 Alley, R. B., D. D. Blankenship, C. R. Bentley, and S. T. Rooney (1986), Deformation of till
741 beneath ice stream B, West Antarctica, *Nature*, 322, 57-59.
- 742 Bamber, J. L., D. G. Vaughan, and I. Joughin (2000), Widespread complex flow in the interior
743 of the Antarctic ice sheet, *Science*, 287, 1248-1250.
- 744 Barenblatt, G. I. (1959), On the equilibrium cracks formed in brittle failure, *Journal of Applied*
745 *Mathematics and Mechanics*, 23(3), 893-900.
- 746 Ben Amar, M., and J. R. Rice (2002), Exact results with the J-integral applied to free-boundary
747 flows, *Journal of Fluid Mechanics*, 461, 321-341.
- 748 Bilby, B. A., and J. D. Eshelby (1968), Dislocations and the theory of fracture, in *Fracture, an*
749 *Advanced Treatise*, vol. II, edited by H. Liebowitz, pp. 99-182, Academic, New York.
- 750 Bilby, B. A., A. H. Cottrell, and K. H. Swinden (1963), The spread of plastic yield from a notch,
751 *Proceedings of the Royal Society A*, 272 (1350), 304314, doi:10.1098/rspa.1963.0055.
- 752 Bindshadler, R. A., and P. L. Vornberger (1990), A VHRR imagery reveals Antarctic ice dy-
753 namics, *Eos*, 71(23).
- 754 Blankenship, D. D., C. R. Bentley, S. T. Rooney, and R. B. Alley (1986), Seismic measurements
755 reveal a porous layer beneath an active Antarctic ice stream, *Nature*, 322, 54-57.
- 756 Blankenship, D. D., C. R. Bentley, S. T. Rooney, and R. B. Alley (1987), Till beneath ice
757 stream B 1. Properties derived from seismic travel times, *Journal of Geophysical Research*, 92,
758 8,903-8,911.
- 759 Catania, G. A., T. A. Scambos, H. Conway, and C. F. Raymond (2006), Sequential stagnation
760 of Kamb Ice Stream, West Antarctica, *Geophysical Research letters*, 33, L14502.

- 761 Cherepanov, G. (1968), Cracks in solids, *International Journal of Solids and Structures*, 4 (8),
762 811-831.
- 763 Clarke, T. S., C. Liu, N. E. Lord, and C. R. Bentley (2000), Evidence for a recently abandoned
764 shear margin adjacent to ice stream B2, Antarctica, from ice-penetrating radar measurements,
765 *Journal of Geophysical Research*, 105, 13,409-13,422.
- 766 Cooper, R. F., and D. L. Kohlstedt (1986), Rheology and structure of olivine-basalt partial melts,
767 *Journal of Geophysical research*, 91, 9315-9323.
- 768 Cuffey, K., and W. S. Paterson (2010), *The physics of glaciers (fourth edition)*, Butterworth-
769 Heinemann.
- 770 Dugdale, D. S. (1960), Yielding of steel sheets containing slits, *Journal of the Mechanics and*
771 *Physics of Solids*, 8, 100-104.
- 772 Durham, W. B., S. H. Kirby, and L. A. Stern (1997), Creep of water ices at planetary conditions:
773 A compilation, *Journal of Geophysical Research*, 102, 16,293-16302.
- 774 Duval, P. (1977), The role of the water content on the creep rate of polycrystalline ice, in *Isotopes*
775 *and impurities in Snow and Ice*, IAHS Publications, 118, 29-33.
- 776 Echelmeyer, K. A., W. D. Harrison, C. Larsen, and J. E. Mitchell (1994), The role of the margins
777 in the dynamics of an active ice stream, *Journal of Glaciology*, 40 (136), 527-538.
- 778 Echelmeyer, K. A., and W. D. Harrison (1999), Ongoing margin migration of Ice Stream B,
779 Antarctica, *Journal of Glaciology*, 45 (150), 361-369.
- 780 Fernandes, M. C., C. R. Meyer, and J. R. Rice (2014), Röthlisberger channel model with anti-
781 plane shear loading superposed on in-plane compression, Abstract C33A-0357 presented at
782 2014 Fall Meeting, AGU, San Francisco, Calif., 15-19 Dec.

- 783 Fisher, J. C. (1951), Calculation of diffusion penetration curves for surface and grain boundary
784 diffusion, *Journal of Applied Physics*, 22 (1), 74-77.
- 785 Goldman, N. L., and J. W. Hutchinson (1975), Fully plastic crack problems: The center-cracked
786 strip under plane strain, *International Journal of Solids and Structures*, 11 (5), 575-591.
- 787 Goldsby, D. L., and D. L. Kohlstedt (2001), Superplastic deformation of ice: Experimental
788 observations, *Journal of Geophysical research*, 106, 11,017-11,030.
- 789 Goldsby, D. L. (2006), Superplastic flow of ice relevant to glacier and ice-sheet mechanics, in
790 *Glacier Science and Environmental Change*, edited by P. G. Knight, Blackwell Publishing.
- 791 Harrison, W. D., K. A. Echelmeyer, and C. Larsen (1998), Measurements of temperature in
792 a margin of Ice Stream B, Antarctica: implications for margin migration and lateral drag,
793 *Journal of Glaciology*, 44 (148), 615-624.
- 794 Haseloff, M. (2015), Modelling the migration of ice stream margins, *PhD thesis*, The University
795 of British Columbia, Canada.
- 796 Iverson, N. R., T. S. Hooyer, and R. W. Baker (1998), Ring-shear studies of till deformation:
797 Coulomb-plastic behavior and distributed strain in glacier beds, *Journal of Glaciology*, 44
798 (148), 634-642.
- 799 Jackson, M., and B. Kamb (1997), The marginal shear stress of Ice Stream B, West Antarctica,
800 *Journal of Glaciology*, 43 (145), 415-426.
- 801 Jacobson, H. P., and C. F. Raymond (1998), Thermal effects on the location of ice stream
802 margins, *Journal of Geophysical research*, 103, 12,111-12,122.
- 803 Joughin, I., S. Tulaczyk, R. Bindshadler, and S. F. Price (2002), Changes in west Antarctic ice
804 stream velocities: Observation and analysis, *Journal of Geophysical research*, 107 (B11), 2289,
805 doi:10.1029/2001JB001029.

- 806 Kamb, B. (1991), Rheological nonlinearity and flow instability in the deforming bed mechanism
807 of ice stream motion, *Journal of Geophysical Research*, 96, 16,585-16,595.
- 808 Kamb, B. (2001), Basal zone of the West Antarctic ice streams and its role in lubrication of their
809 rapid motion, *Antarctic Research Series*, 77, 157-199.
- 810 Kubo, S., K. Ohji, and K. Ogura (1979), Analysis of creep crack-propagation on the basis of the
811 plastic singular stress-field, *Engineering Fracture Mechanics*, 11 (2), 315-329.
- 812 Kyrke-Smith, T. M., R. F. Katz, and A. C. Fowler (2014), Subglacial hydrology and the formation
813 of ice streams, *Proceedings of the Royal Society A*, 470: 20130494.
- 814 Kyrke-Smith, T. M., R. F. Katz, and A. C. Fowler (2015), Subglacial hydrology as a control on
815 emergence, scale, and spacing of ice streams, *Journal of Geophysical Research*, 120, 1501-1514.
- 816 Landes, J. D., and J. A. Begley (1976), A fracture mechanics approach to creep crack growth, in
817 *Mechanics of Crack Growth*, edited by J. R. Rice and P. C. Paris, pp. 128-148, Amer. Soc. for
818 Testing and Materials (ASTM), Special Technical Publication (STP) 590, Philadelphia.
- 819 Lliboutry, L. A., and P. Duval (1985), Various isotropic and anisotropic ices found in glaciers
820 and polar ice caps and their corresponding rheologies, *Annales Geophysicae*, 3, 207-224.
- 821 McMeeking, R. M., and R. E. Johnson (1986), On the mechanics of surging glaciers, *Journal of*
822 *Glaciology*, 32 (110), 120-132.
- 823 Nye, J. F. (1953), The flow law of ice from measurements in glacier tunnels, laboratory exper-
824 iments and the Jungfraufirn borehole experiment, *Proceedings of the Royal Society A*, 219,
825 477-489.
- 826 Perol, T., and J. R. Rice (2011), Control of the width of West Antarctic ice streams by internal
827 melting in the ice sheet near the margins, Abstract C11B-0677 presented at 2011 Fall Meeting,
828 AGU, San Francisco, Calif., 5-9 Dec.

- 829 Perol, T., and J. R. Rice (2015), Shear heating and weakening of the margins of West Antarctic
830 ice streams, *Geophysical Research Letters*, doi:10.1002/2015GL063638.
- 831 Perol, T., J. R. Rice, J. D. Platt, and J. Suckale (2015), Subglacial hydrology and ice stream
832 margin locations, *Journal of Geophysical Research*, 120, doi:10.1002/2015JF003542.
- 833 Raymond, C. F. (1996), Shear margins in glaciers and ice sheets, *Journal of Glaciology*, 42 (140),
834 90-102.
- 835 Raymond, C. F., K. A. Echelmeyer, I. M. Whillans, and C. S. M. Doake (2001), Ice stream shear
836 margins, *Antarctic Research Series*, 77, 137-155.
- 837 Rempel, A. W. (2009), Effective stress profiles and seepage flows beneath glaciers and ice sheets,
838 *Journal of Glaciology*, 55 (191), 431-443.
- 839 Rice, J. R. (1967), Stresses due to a sharp notch in a work-hardening elastic-plastic material
840 loaded by longitudinal shear, *Journal of Applied Mechanics*, 34, 287-298.
- 841 Rice, J. R. (1968a), A path independent integral and the approximate analysis of strain concen-
842 tration by notches and cracks, *Journal of Applied Mechanics*, 35, 379-386.
- 843 Rice, J. R. (1968b), Mathematical analysis in the mechanics of fracture, in *Fracture, an Advanced*
844 *Treatise*, vol. II, edited by H. Liebowitz, pp. 191-311, Academic, New York.
- 845 Röthlisberger, H. (1972), Water pressure in intra- and subglacial channels, *Journal of Glaciology*,
846 11 (62), 177-203.
- 847 Scambos, T. A., K. A. Echelmeyer, M. A. Fahnestock, and R. A. Bindschadler (1994), Devel-
848 opment of enhanced ice flow at the southern margin of Ice Stream D, Antarctica, *Annals of*
849 *Glaciology*, 20, 313-318.
- 850 Schoof, C. (2004), On the mechanics of ice-stream shear margins, *Journal of Glaciology*, 50, 169,
851 208-218.

- 852 Schoof, C. (2010), Ice-sheet acceleration driven by melt supply variability, *Nature*, 468, 803-806.
- 853 Schoof, C. (2012), Thermally driven migration of ice-stream shear margins, *Journal of Fluid*
854 *Mechanics*, 712, 552-578.
- 855 Schulson, E. M., and P. Duval (2009), Creep and fracture of ice, *Cambridge University Press*.
- 856 Shabtaie, S., and C. R. Bentley (1987), West Antarctic ice streams draining into the Ross ice
857 shelf: Configuration and mass balance, *Journal of Geophysical research*, 92, 1311-1336.
- 858 Shabtaie, S., and C. R. Bentley (1988), Ice-thickness map of the West Antarctic ice streams by
859 radar sounding, *Annals of Glaciology*, 11, 126-136.
- 860 Shreve, R. L. (1972), Movement of water in glaciers, *Journal of Glaciology*, 11 (62), 205-214.
- 861 Suckale J., J. D. Platt, T. Perol, and J. R. Rice (2014), Deformation-induced melting in the
862 margins of the West Antarctic ice streams, *Journal of Geophysical research*, 119, 1004-1025.
- 863 Tulaczyk, S., W. B. Kamb, and H. F. Engelhardt (2000), Basal mechanics of Ice Stream B, West
864 Antarctica 1. Till mechanics, *Journal of Geophysical research*, 105, 463-481.
- 865 van der Veen, C. J., and I. M. Whillans (1996), Model experiments on the evolution and stability
866 of ice streams, *Annals of Glaciology*, 23, 129-137.
- 867 Weertman, J. (1972), General theory of water flow at the base of a glacier or ice sheet, *Reviews*
868 *of Geophysics and Space Physics*, 10, 287-333.

Parameter	Units	Value
Ice stream width, W	km	34
Ice sheet thickness, H	km	1
Ice sheet slope, S	–	0.0012
Basal shear stress beneath ice stream, τ_{base}	kPa	3.5
Gravitational acceleration, g	m s^{-2}	9.81
Density of ice, ρ_{ice}	kg m^{-3}	917
Density of water, ρ_w	kg m^{-3}	1000
Latent heat per unit mass, L	kJ/kg	335
Friction coefficient, f	–	0.6
Gauckler-Manning coefficient, n_m	$\text{s m}^{-1/3}$	0.01

Table 1. A table showing the parameters used in this paper. The values of ice thickness, ice stream width, and slope are intended to model ice stream B2 [Joughin *et al.*, 2002]. As shown in the text, these parameters cannot be varied independently, and variations in these parameters only alter the stress around the locking point through J_{tip} .

Pre-factor, A	Stress exponent, n
$2.4 \times 10^{-14}, \text{Pa}^{-1} \text{s}^{-1}$	1
$2.4 \times 10^{-24}, \text{Pa}^{-3} \text{s}^{-1}$	3
$2.2 \times 10^{-30}, \text{Pa}^{-4} \text{s}^{-1}$	4

Table 2. A table showing the parameters for the three different power law rheologies used in this paper. The rheology with $n = 3$ is Glen’s law and we use the recommended value of A at 0 °C from Cuffey and Paterson [2010]. The $n = 4$ rheology is based upon the dislocation creep experiments rheology proposed in Durham *et al.* [1997] and is expected to dominate at the highest stresses.

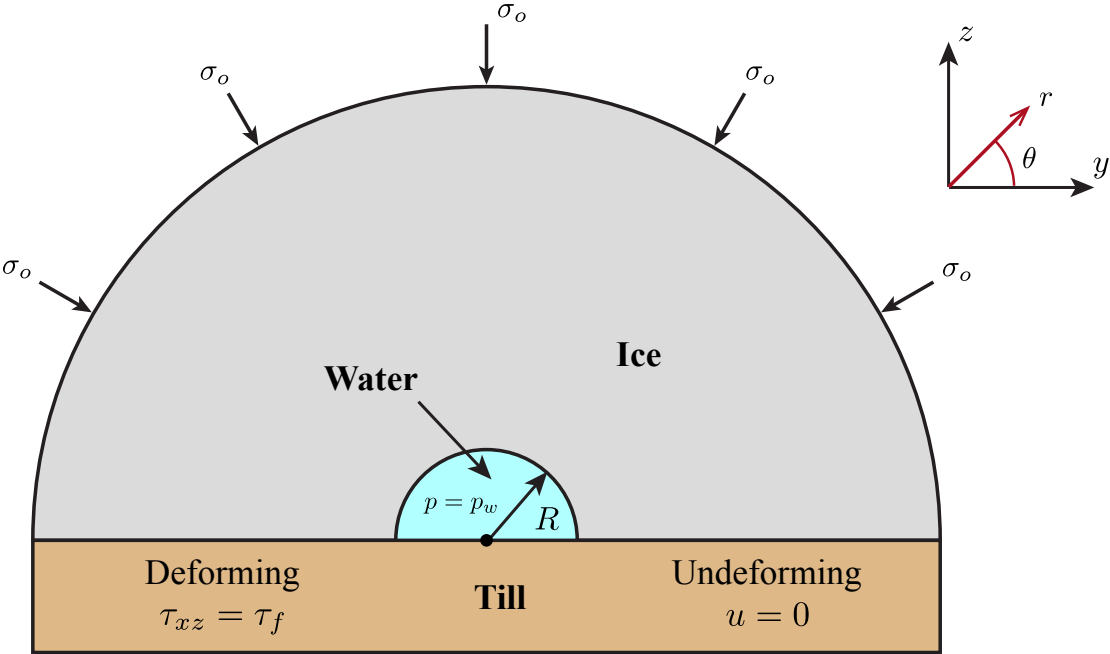


Figure 1. A sketch of the geometry used in our calculations for the deformation around the channel. We assume a semi-circular channel with a radius R incised into the ice, which rests upon a subglacial till layer. The anti-plane strain rates are calculated assuming that the bed is deforming to the left of the channel, and undeforming to the right of the channel. We model the creep closure of the channel using the pressure difference between the channel operating at a pressure p and the ice overburden σ_o .

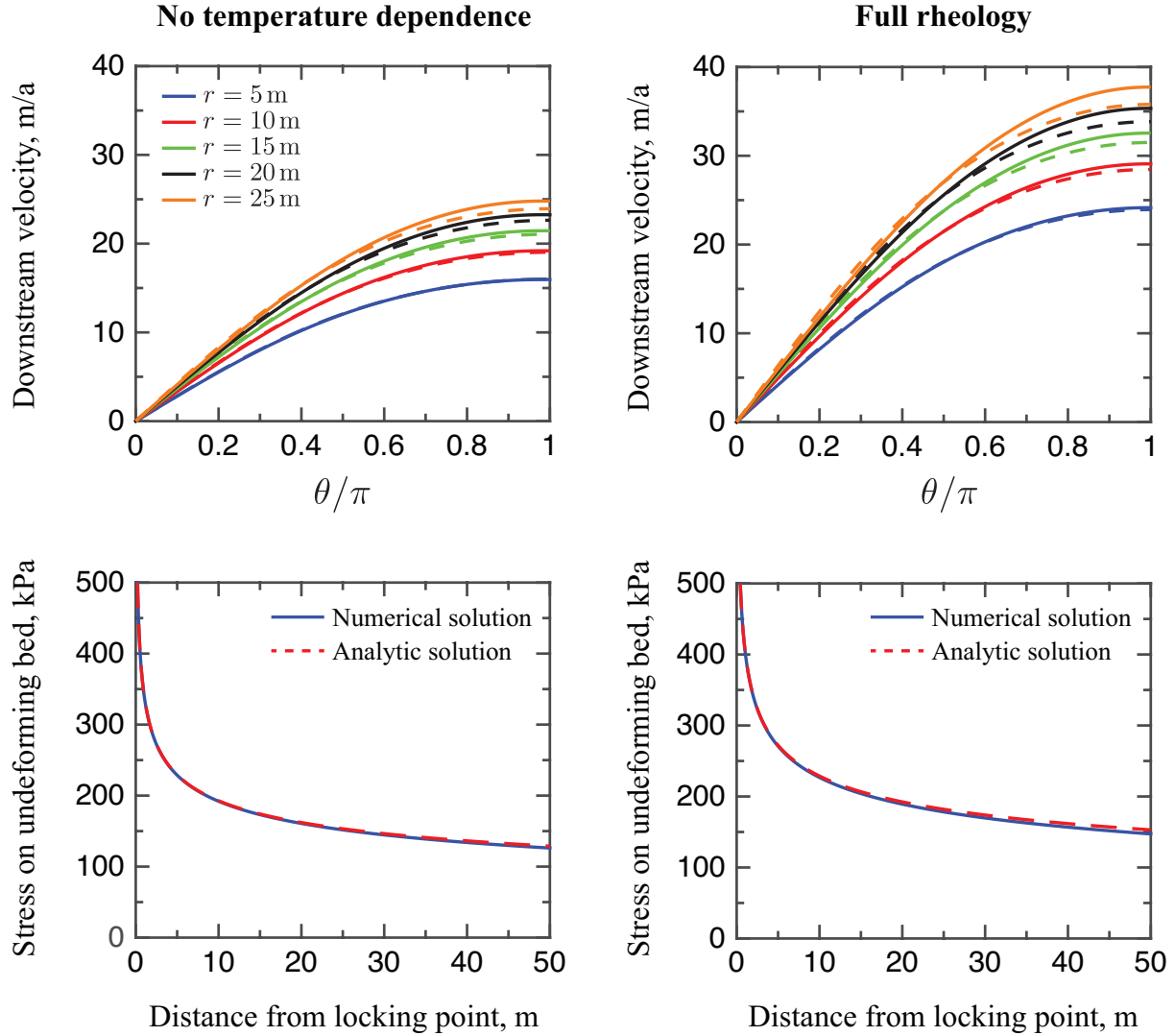


Figure 2. A plot comparing the analytic solution given in equation (A24) valid right at the locking point and numerical simulations generated using the finite element package COMSOL for the whole ice stream model from *Perol et al.* [2015]. The left hand column shows simulations that assume a constant viscosity and the right hand column shows simulations that couple deformation and temperature through a temperature dependent rheology as described in *Perol et al.* [2015]. The upper panels show the downstream velocity as a function of θ for a range of r and the lower panels shows the stress concentrated on the undeforming bed. The curve at $r = 5$ m is used to infer a best-fitting value of J_{tip} that is then used to fit all remaining curves. We see good agreement between the analytic and numerical solutions for several tens of meters, allowing us to make a small-scale yielding approximation.

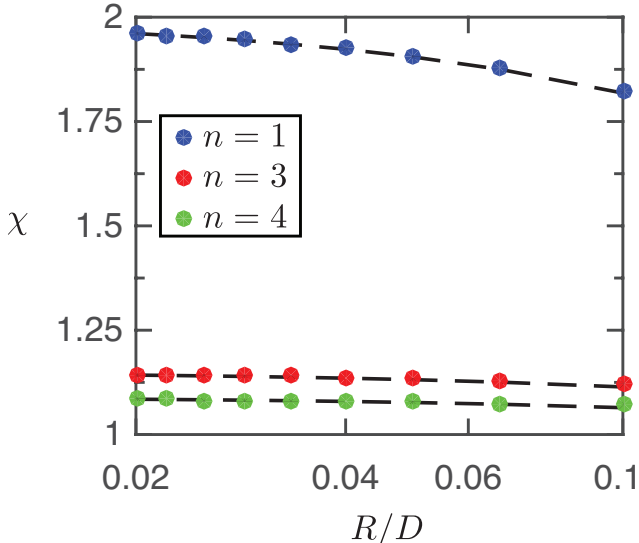


Figure 3. A plot of χ against R/D for $n = 1$, $n = 3$, and $n = 4$, alongside the fitting function $\chi = \chi_{inf}(1+R/D)^{-1/n}$. This plot allows us to infer values of χ_{inf} that are then used to determine the maximum stress resolved on the undeforming bed. We find best fitting values of χ_{inf} to be 2 for $n = 1$, 1.15 for $n = 3$, and 1.09 for $n = 4$.

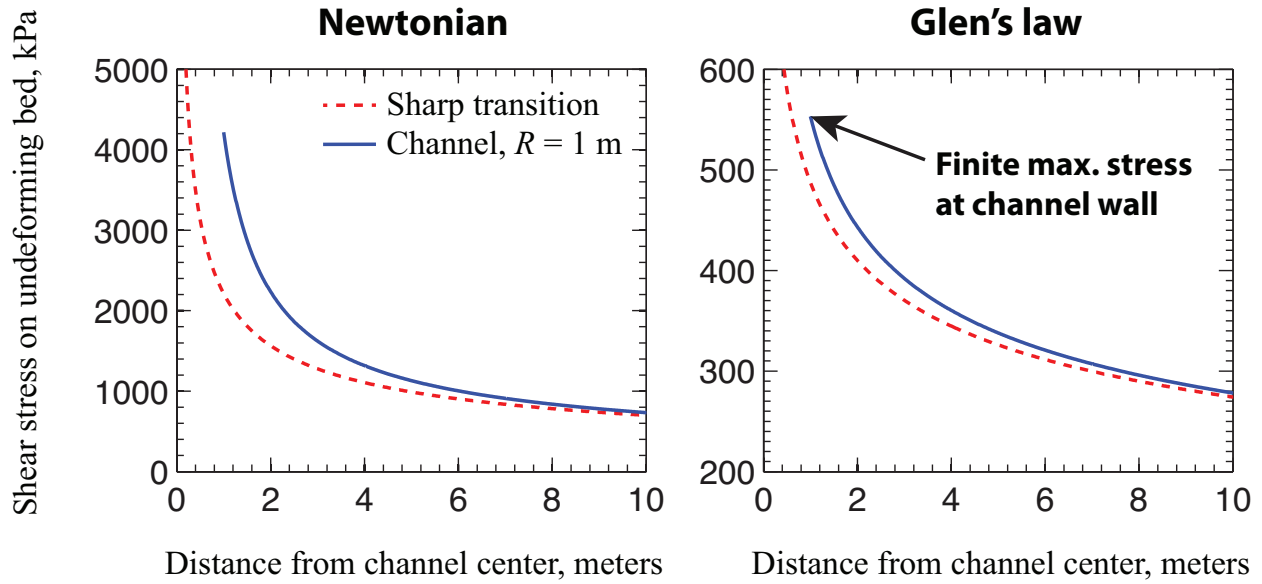


Figure 4. A plot showing the maximum stress on the undeforming bed accounting for the channel in blue alongside the prediction using the solution for a sharp margin given in equation (4) for $n = 1$ and $n = 3$. We see that the Newtonian rheology leads to significantly higher shear stresses on the bed than the Glen’s law rheology, and that the solution for a sharp margin provides a reasonable approximation to the stress field accounting for the channel for all y .

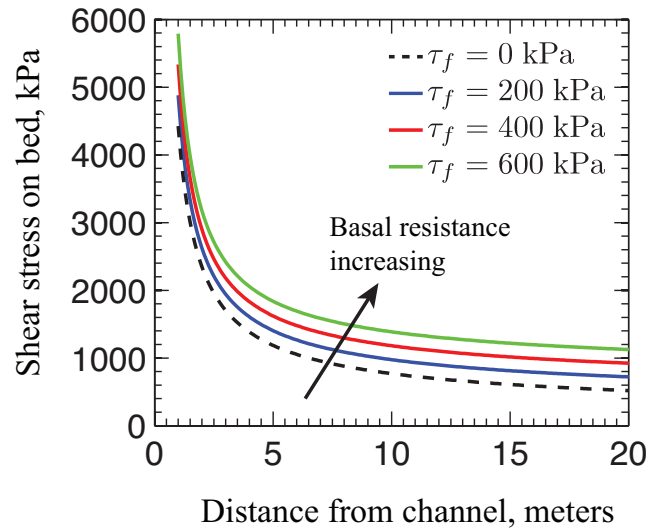


Figure 5. A plot showing how the stress on the undeforming bed varies with the basal resistance of the deforming bed τ_f for the parameters in Table 1 and $n = 1$. Our results show that for these parameter choices the dependence of maximum stress on τ_f is not significant. However, as discussed in Section 4.3, we expect the role of τ_f to become more important as τ_f becomes comparable to $\tau_{sharp}(R)$.

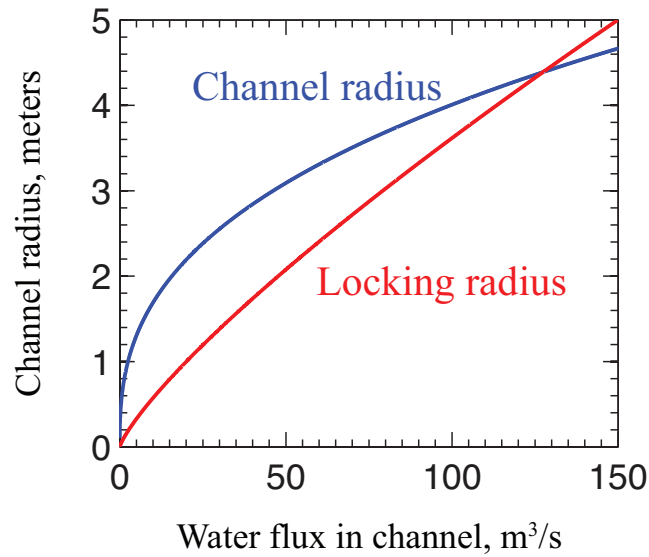


Figure 6. A plot of the channel radius R and locking radius R_{lock} against the water flux in the channel for the parameters in Tables 1 and 2 assuming a Glen’s law rheology. We see that $R < R_{lock}$ – and thus a stable margin configuration exists – whenever the water flux exceeds a critical value of $\sim 127 \text{ m}^3/\text{s}$. This water flux corresponds to a channel with a radius of 4 m.

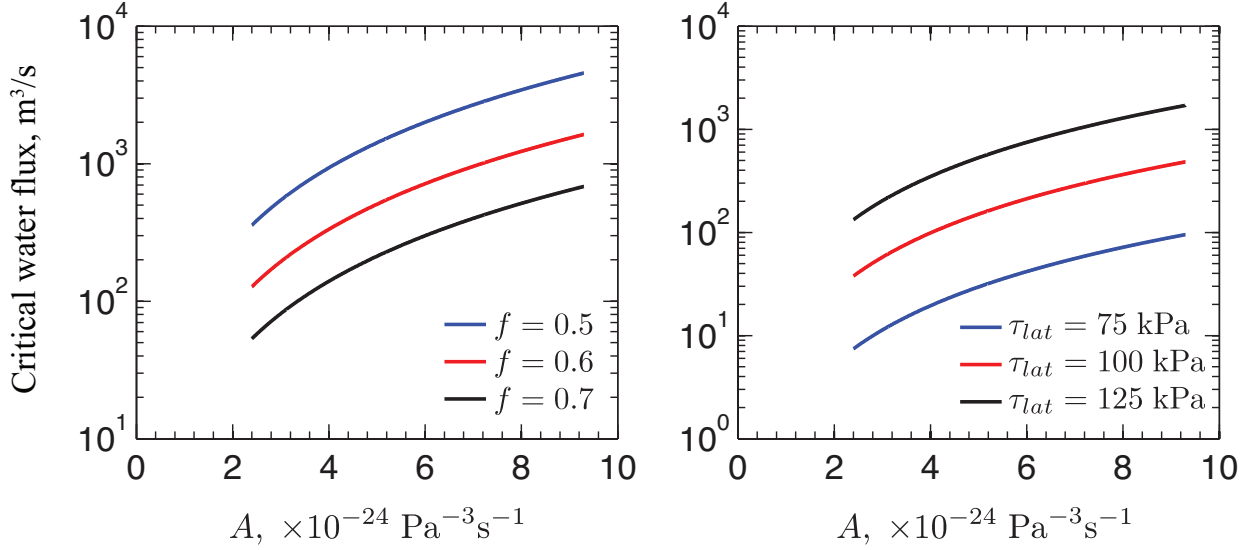


Figure 7. A plot showing how the critical water flux Q_{lock} varies for a Glen’s law rheology across the range of values for A at 0 °C outlined in *Cuffey and Paterson* [2010] for different values of f and τ_{lat} . These plots were produced using the parameters in Tables 1 and 2. We see significant variability with A with higher values of A leading to larger critical fluxes. This sensitive dependence on the poorly constrained A makes it hard to predict values of Q_{lock} .

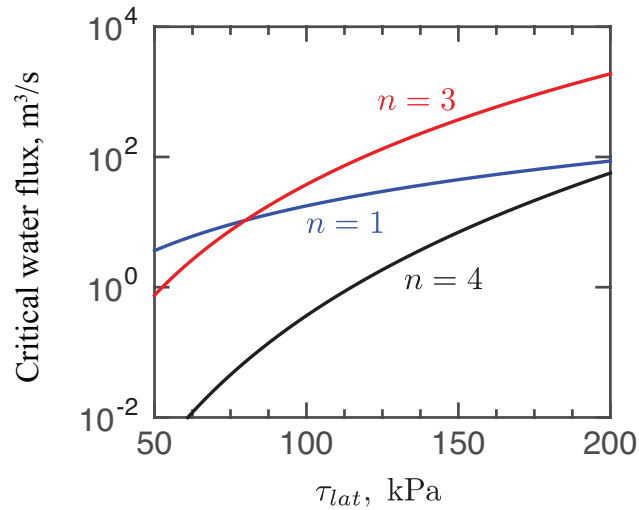


Figure 8. A plot of the critical water flux Q_{lock} against the average stress supported at the shear margin τ_{lat} for $n = 1$, $n = 3$, and $n = 4$. This plot was produced using the parameters in Tables 1 and 2. We see that Q_{lock} increases rapidly with τ_{lat} . Note that the $n = 4$ curve predicts much lower critical water fluxes than $n = 1$ and $n = 3$.

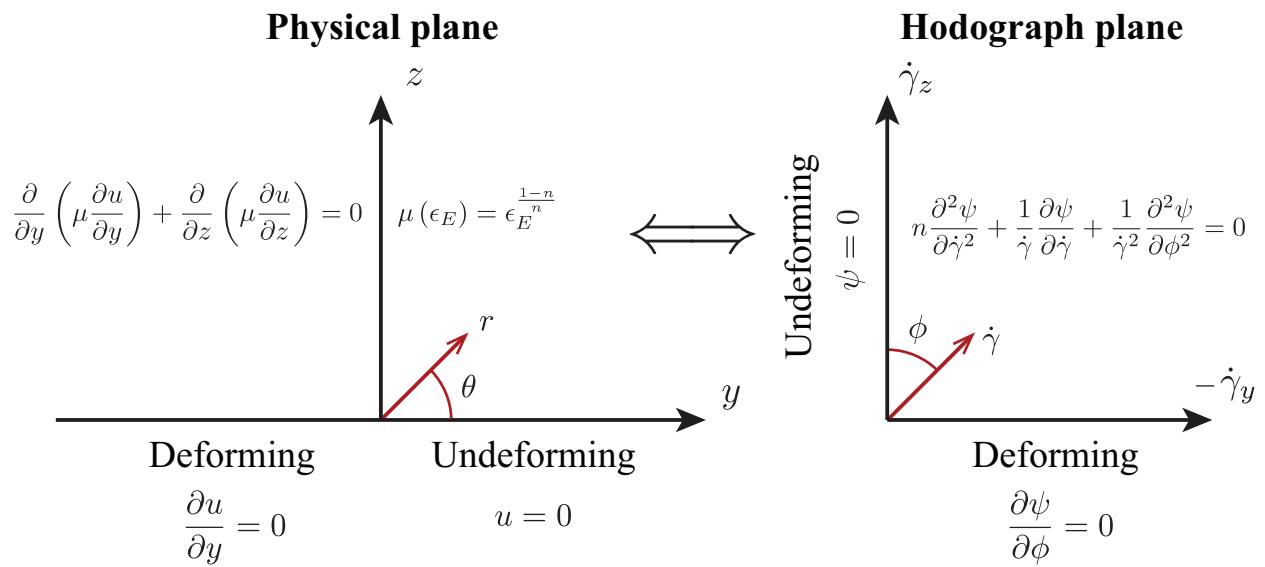


Figure 9. A sketch of the physical plane and hodograph plane used in Appendix A showing the equations solved, boundary conditions used, and coordinates in both planes.